Late-glacial and Holocene history of the northeast Mediterranean mountain glaciers - New insights from in situ -produced 36Cl - based cosmic ray exposure dating of paleo-glacier deposits on Mount Olympus, Greece

Michael Styllas, Irene Schimmelpfennig, Lucilla Benedetti, Matthieu Ghilardi, Georges Aumaitre, Didier Bourlès, Karim Keddadouche

▶ **To cite this version:**

Michael Styllas, Irene Schimmelpfennig, Lucilla Benedetti, Matthieu Ghilardi, Georges Aumaitre, et al.. Late-glacial and Holocene history of the northeast Mediterranean mountain glaciers - New insights from in situ -produced 36Cl - based cosmic ray exposure dating of paleo-glacier deposits on Mount Olympus, Greece. Quaternary Science Reviews, 2018, 193, pp.244-265. 10.1016/j.quascirev.2018.06.020 . hal-01832838

HAL Id: hal-01832838
https://hal.science/hal-01832838v1

Submitted on 2 May 2019

HAL is a multi-disciplinary open access archive for the deposit and dissemination of scientific research documents, whether they are published or not. The documents may come from teaching and research institutions in France or abroad, or from public or private research centers.

L'archive ouverte pluridisciplinaire **HAL**, est destinée au dépôt et à la diffusion de documents scientifiques de niveau recherche, publiés ou non, émanant des établissements d'enseignement et de recherche français ou étrangers, des laboratoires publics ou privés.

Late-glacial and Holocene glacial history of the northeast Mediterranean mountain glaciers - New insights from *in situ*-produced ^{36}Cl-based cosmic ray exposure dating of paleo-glaciers deposits on Mount Olympus, Greece

Michael N. Styllas[1], Irene Schimmelpfennig[2], Lucilla Benedetti[2], Mathieu Ghilardi[2] and ASTER Team[2*]

[1] GEOSERVICE LTD, Thessaloniki, Greece
[2] Aix Marseille Univ, CNRS, IRD, INRA, Coll France, CEREGE, Aix-en-Provence, France

* Georges Aumaître, Didier Bourlès, Karim Keddadouche.

Abstract

In this study, we present a new glacial chronology based on 20 *in situ*-produced ^{36}Cl-based cosmic ray exposure datings from moraine boulders and bedrock from the Throne of Zeus (TZ) and Megala Kazania (MK) cirques on Mount Olympus. The ^{36}Cl derived ages of glacial landforms range from 15.6 ± 2.0 to 0.64 ± 0.08 ka, spanning the Late-glacial and the Holocene. The Late-glacial, recorded in both cirques, is partitioned in three distinct phases (LG1-3): an initial phase of moraine stabilization at 15.5 ± 2.0 ka with subsequent deglaciation starting at ~14 ka (LG1), followed by a shift to marginal conditions for glaciation at 13.5 ± 2.0 ka (LG2), sustained by large amounts of wind-blown snow, despite regional warming. Glacial conditions returned at 12.5 ± 1.5 ka (LG3) and were characterized by low air temperatures and glacier shrinking. The Holocene glacial phases (HOL1-3) are recorded only in the MK cirque, likely due to its topographic attributes. An early Holocene glacier stillstand (HOL1) at 9.6 ± 1.1 ka follows the regional temperatures recovery. No glacier activity is observed during the mid-Holocene. The Late Holocene glacier expansions, include a moraine stabilization phase (HOL2) at 2.5 ± 0.3 ka, during wet conditions and solar insolation minima, while (HOL3) corresponds to the early part of the Little Ice Age (0.64 ± 0.08ka). Our glacial chronology is coherent with glacial chronologies from several cirques along the northeast Mediterranean mountains and in pace with numerous proxies from terrestrial and marine systems from the north Aegean Sea.

Keywords

Small cirque glaciers;
In situ produces cosmogenic ^{36}Cl;
Surface Exposure Dating (SED);
Glacial phases;
Late-glacial;
Holocene;
Northeast Mediterranean;
Mount Olympus;
Greece.

1. Introduction

Glaciers are very good indicators of climate change due to their mass balance sensitivity to variations in precipitation, temperature and solar insolation (Oerlemans, 2005). Therefore, the knowledge of the history of mountain glaciers, as recorded in a variety of glacial landforms, allows for reconstruction of local and regional paleoclimatic conditions. Glaciers usually form above the local climate-dependent equilibrium line altitude (ELA). In climates that are marginal for glaciation, like the ones found in Mediterranean mountains, small cirque glaciers are often formed in protected locations in response to local topoclimatic factors such as excess snow accumulation through the deposition of wind-blown and avalanching snow (e.g. Hughes et al., 2006). Under these conditions, small cirque glaciers can even occur at elevations lower than the ELA, when the accumulation rates are four times higher than the local precipitation (e.g. González Trueba et al., 2008; Hughes, 2009, Huss and Fischer, 2016 and references therein). The advance, stabilization and retreat phases of these small cirque glaciers can thus be triggered by local topoclimatic factors as well as by variations in the regional climate, making them overall invaluable, albeit discontinuous, recorders of past climate variability.

The Mediterranean basin with its mid-latitudinal position and its proximity to the North Atlantic, Eurasian and North African climatic regimes, has undergone significant changes in the terrestrial and marine systems during the late Pleistocene, and this is also reflected in the glacial records of the Mediterranean mountains (e.g. Kuhlemann et al., 2008, Hughes and Woodward, 2008, 2016). The glacial history of the mountains surrounding the Mediterranean basin has been conceived as one of the best recorders of ocean-continent climate interactions and their external forcing mechanisms during periods of major glacier advances as the Last Glacial Maximum – LGM (e.g. Kuhlemann et al., 2008; Domíniguez-Villar et al., 2013). To a smaller geographical extent, the sub-region of the northeast Mediterranean (southern Balkans, north Aegean and Marmara Seas, Fig. 1), has been also characterized by complex Late Pleistocene and Holocene marine and terrestrial environmental dynamics, as it comprises a transition region where W-E and N-S contrasting climatic and hydrological regimes collide and interact with each other (e.g. Lawson et al., 2005, Digerfeldt et al., 2007, Kothoff et al., 2008, Marino et al., 2009, Pross et al., 2009, Tzedakis et al., 2009, Schmiedl et al., 2010, Francke et al., 2013, Zhang et al., 2014, Styllas and Ghilardi, 2017, Koutsodendris et al., 2017).

The recent advances in surface exposure dating (SED) techniques of glacial landforms using *in situ*-produced cosmogenic nuclides such as beryllium-10 (^{10}Be) and chlorine-36 (^{36}Cl) (e.g. Balco, 2011), have resulted in an increasing number of studies that have considerably improved our understanding of the Late Pleistocene glacial extents and timing of Mediterranean mountains (Hughes and Woodward, 2017 and references there in). In the late 1990's Mount Olympus, Greece's highest mountain, saw one of the earliest attempts for dating glacial deposits along the Mediterranean mountains using ^{36}Cl (Manz, 1998). The results of more recent studies that followed this pioneering attempt, suggest that the Mediterranean paleoglaciers generally advanced during two periods after the global LGM (*c*. 27.5–23.3ka, Hughes and Gibbard, 2015), confined between 16-15 ka and 13-10 ka, and in phase with the GS-2a and GS-1 stadials in the Greenland oxygen isotope record (Ribollini et al., 2017 and references therein).

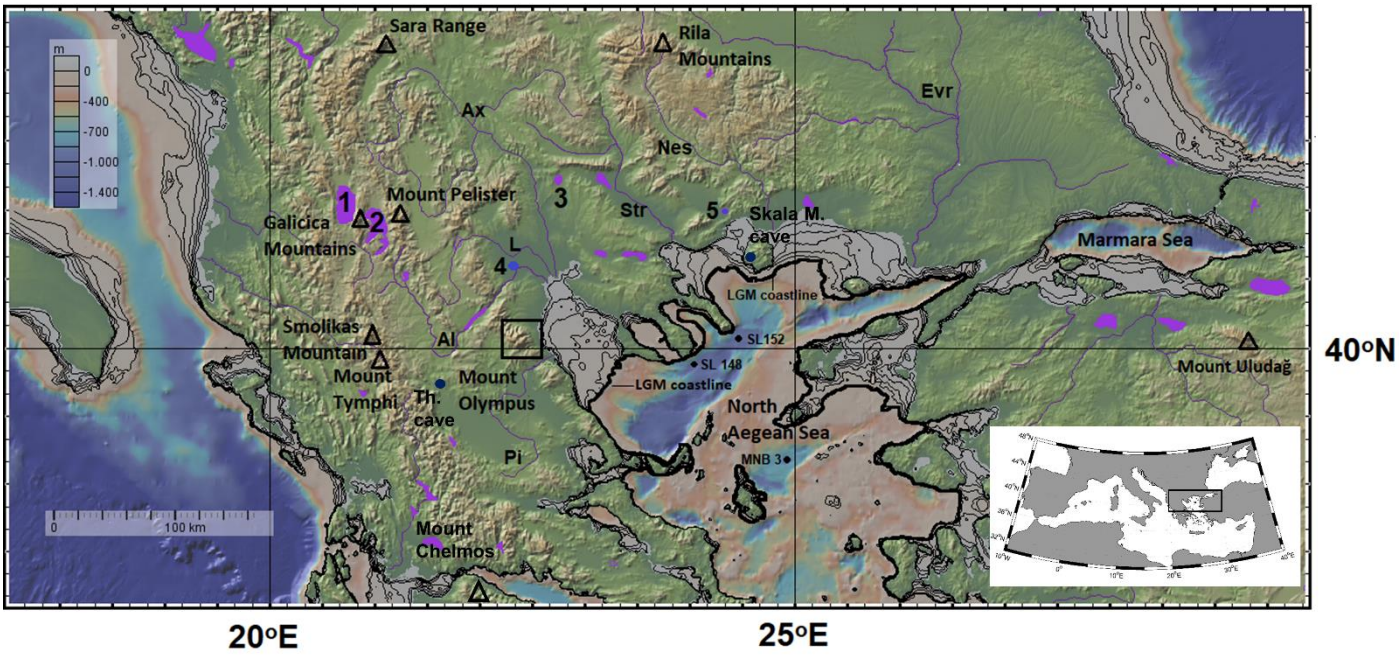

Fig. 1. Location of the study area (black rectangle) and of the northeast Mediterranean mountains (black triangles) where cosmogenic surface exposure dating of glacial landforms (SED), or glacier equilibrium line altitude (ELA) reconstrunctions are available since the Last Glacial Maximum (LGM). Purple areas correspond to major lakes, while more specifically, numbers 1, 2, 3, 4 and 5 correspond to Lakes Ohrid, Prespa, Dorjan, Loudias and Tenaghi Phillipon swamp. Also shown are the main fluvial systems discharging into the north Aegean Sea (Pi: Pinios River, Al: Aliakmon River, L: Loudias River, Ax: Axios River, Str: Strymonas River, Nes: Nestos and Evr: Evros/Meriç River). Blue circles show the locations of speleothem and sediment cave records (Th: Theopetra Cave, Duhlata Cave, Skala M: Skala Marion Cave). The locations of north Aegean marine cores SL 152, SL 148 and MNB 3 are also shown (black dots). The bathymetric contours between -120 and -20m, representing the LGM (thick black line) and early Holocene coastlines, are also shown. Topographic and bathymetric background is provided by Geomapapp® (http://www.geomapapp.org, Ryan et al., 2009).

Accordingly, during the last decade, an augmented volume of research based on geomorphological evidence, paleoclimatic reconstrunctions and SED of glacial deposits and landforms, allowed assessing a general framework of the glacial evolution of the southern Balkan and northwestern Turkey mountains during the LGM and the Late Glacial (e.g. Pindos Range: Tymphi Mountain and Mount Smolikas – Hughes et al., 2006, Sara Range – Kuhlemann et al., 2009, Mount Uludağ - Zahno et al., 2010, Rila Mountains - Kuhlemann et al., 2013, Mount Chelmos – Pope et al., 2015, Mount Pelister – Ribollini et al., 2017, Galicica Mountains – Gromig et al., 2017, Fig. 1). With the exception of Mount Uludağ in NW Anatolia, the number of SED studies in the northeast Mediterranean mountains is, however, still limited and does not provide a well-constrained glacial chronology.

Despite the fact that glaciers are uncommon in Greece, we present here for the first time a glacier chronology spanning the Late-glacial and the Holocene, derived from ^{36}Cl in situ cosmogenic dating of two small (< 0.5km^2) cirque glaciers on Mount Olympus, based on 20 rock samples from bedrock and glacially transported boulders (Fig. 2). Our glacial chronology is compared to the existing SED studies from glacial cirques situated along the headwaters of the northeast Mediterranean Sea (north Aegean and Marmara seas), in an effort to reconstruct a regional and robust signal of glacier fluctuations. By correlating our findings with well-studied terrestrial (lacustrine, fluvial sequences and speleothems) and marine records from the same region (Fig. 1), we interpret our new glacier chronology in terms of external and the underlying local and regional climate forcing. The density of sampled boulders in Megala Kazania cirque further allows us to propose a chronology of glacier oscillations, to depict paleoclimatic information and to correlate the findings with glacier and other proxy records from other northeast Mediterranean.

2. Climatic and glacio-geomorphic setting of Mount Olympus

2.1 Past and present climatic conditions

Mount Olympus is a coastal massif of circular shape, composed of Triassic and Cretaceous carbonate sequences, rising 2918m above the northwestern Aegean Sea coastline (Fig. 1, Fig. 2 inset map). Its

proximity to the sea as expressed by the short distance (18km) of its highest peaks from the shore, has a pronounced impact on the local climate, with increased supply of moisture and high precipitation and temperature gradients (Styllas et al., 2016).

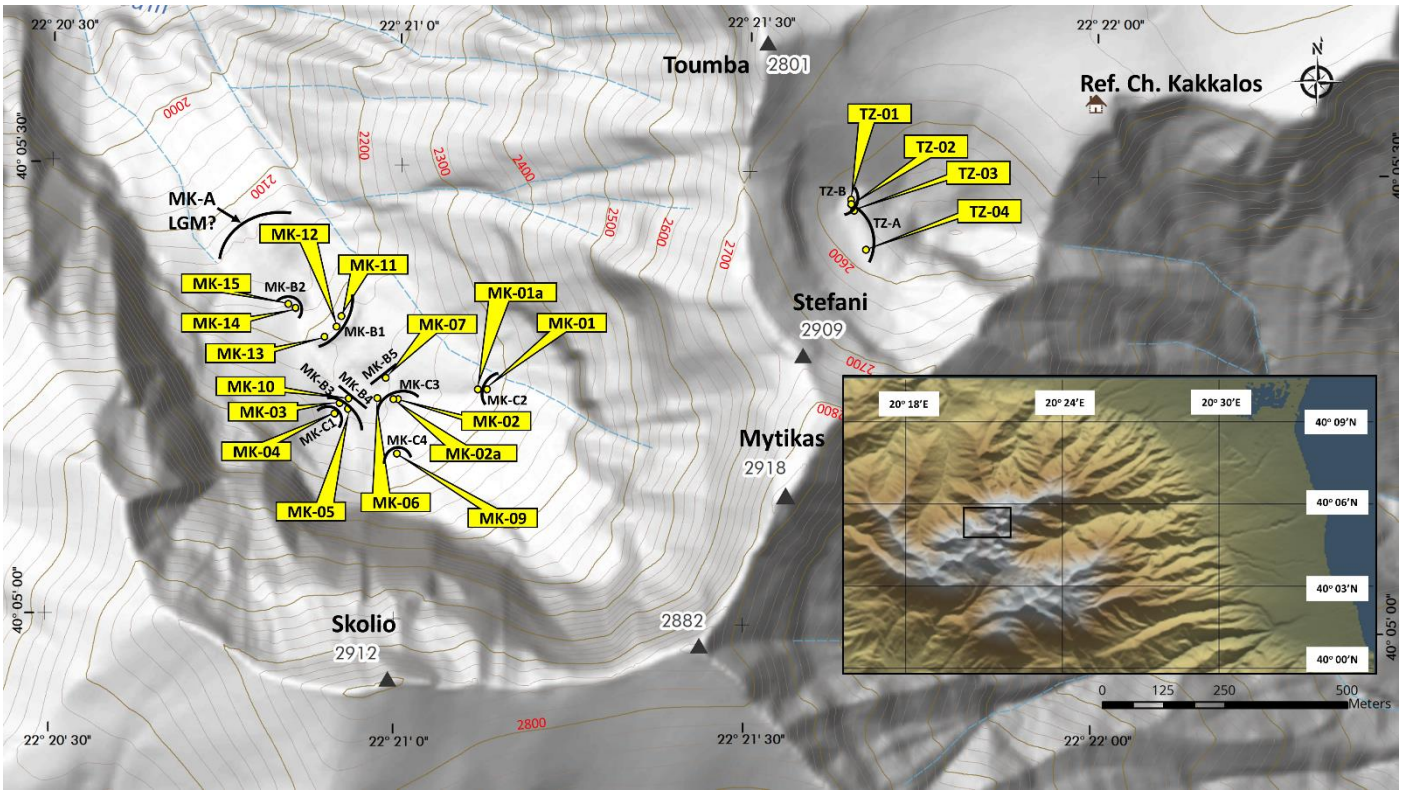

Fig. 2. Locations of the respective groups of moraines (MK-A, MK-B1-5, MK-C1-4, TZ-A and TZ-B), illustrated with black curved lines and of the boulder and bedrock samples (*n=20*), illustrated in yellow dots and boxes selected for *in situ*-produced ^{36}Cl-based cosmic ray exposure dating from the Throne of Zeus (TZ) and Megala Kazania (MK) cirques. (DEM source: Ktimatologio A.E. Elevation contours provided from RouteMaps.gr, Inset map data: SRTM 90).

The high plateaus and valleys of Mount Olympus exhibit a variety of glacial and periglacial landforms and deposits, testifying to the recurrent presence of Pleistocene glaciations, which tentatively have been ascribed to the marine isotope stages (MIS) 8, 6 and 4-2 (Smith et al., 1997). During the first stage of the last glaciation (Würmian MIS 4-2), the snowline was depressed down to 1300m, and during the latter stage of MIS 2 (LGM) it was confined within the upland cirques at elevations higher than 2000m (Smith et al., 1997, 2006). Within one of these cirques, the Megala Kazania cirque, extant permanent snowfields and ice bodies under the scree slopes have been considered remnants of the final Late Holocene deglaciation, which most likely occurred after the Little Ice Age (Styllas et al., 2016).

During the LGM, the overall conditions in the vicinity of Mount Olympus were substantially different, as the sea-level of the Aegean Sea was 120m lower (Lambeck 1996), and large portions of the present day continental shelves were exposed subaerialy (Perissoratis and Conispoliatis, 2003), reducing significantly the overall water surface area of north Aegean Sea (Fig. 1). The LGM Aegean Sea Surface Temperatures (SST's) were 6^{o}C lower compared to present values (Kuhlemann et al., 2008), and the local ELA was at 2000 ±150m; a depression that resulted from a significant drop (~7–9^{o}C) in air temperatures (Peyron et al., 1998, Kuhlemann et al. 2008). In a study by Styllas et al., (2016), geomorphological evidence and Holocene paleoclimatic simulations for Megala Kazania cirque, based on projected values of annual precipitation (P_{ann}) and summer temperature (T_s) from a proximal (13km to the north) meteorological station, suggest that the best candidates for a glacier to exist and/or to advance with the local ELA[1] at 2200m, are P_{ann} = 2160 ±160mm and T_s = 4.6 ± 0.4^{o}C. These values are very similar to the ones found (P_{ann} = 2300 ± 200mm and T_s = 4.9^{o}C) for the local glacial maximum of Pindos Mountains (Mount Tymphi, Fig. 1) during the Tymphian (28.2 – 24.3 ka BP) cold stage (Hughes et al., 2003, 2006a, 2008). Therefore, one would expect that the considerable drop in air temperatures (~7^{o}C) during the LGM would have resulted in a significant drop in the local ELA, in both Mount Olympus and Mount Tymphi, but the reconstructed drop in the local ELA

[1] Given the small vertical range (~200m) and size (<0.5km^2) of TZ and MK glaciers, we consider that the observed frontal moraines elevation coincides with the local ELA.

derived from a regional synthesis for the entire Mediterranean Basin, was only 200m (Kuhlemann et al., 2008). This can be explained by the fact that during the LGM, both Mount Olympus and Mount Tymphi were out of the zone of major Mediterranean cyclone tracks, which were deflected either further north towards the Adriatic basin and the western Balkans, or further south towards the eastern Mediterranean and resulted in drier conditions over the northeast Mediterranean (Kuhlemann et al., 2013 and references therein). The presence of rock glaciers on Mount Tymphi down to 1800m is consistent with the LGM temperature depressions and moisture deficiency (Hughes et al., 2003). Superimposed on the LGM atmospheric circulation patterns of low cyclonic activity over the southern Balkans and the Aegean Sea, was the fact that during the LGM Mount Olympus was distanced 100km from the coastline (Fig. 1). Potentially, the distant cold waters and the overall reduced water surface area of the north Aegean Sea, also resulted in moisture deficit and reduced precipitation, conditions more representative of a continental setting that was restrictive to large glacier expansions. Therefore, the altitudinal extent of our study sites, is confined above the reconstructed LGM ELA (2000 ±150m, moraine MK-A, Fig. 2) and is considered to correspond to the range of Late-glacial and Holocene ELAs.

At present, the distribution of precipitation in the vicinity of Mount Olympus varies with altitude and distance from the coast, as the highest peaks constitute an orographic barrier, which results in a climatic partition between the eastern (marine) and western (continental) sides of the mountain (Styllas et al., 2016). Along the eastern and western piedmonts and at elevations between 50-150m, annual precipitation (P_{ann}) and temperature (T_{ann}) are 550mm and 15^{o}C respectively, whereas closer to the mountain and at elevations between 400 and 800m, P_{ann} reaches 600–800mm and T_{ann} is 9.9^{o}C (Styllas et al., 2016). The eastern (marine) side of Mount Olympus receives on average 200mm more precipitation than the western (continental) side (period of observations 1960 – 2000, Styllas et al., 2016). Above 1500m, most of the winter (December - March) precipitation occurs as snow, and in depressions below the highest peaks, including the cirques under consideration, the snowpack thickness reaches excess values of 1.5m. Mean summer (June – September) temperatures recorded in the meteorological station of refuge Christos Kakkalos (Fig., 2, period of observations 2007 – 2016), range between 8.5 and 10.5^{o}C. Winter precipitation (P_w) on Mount Olympus is mainly related to cyclogenesis over the Aegean Sea and central Mediterranean (e.g. Flockas et al., 1996, Batzokas et al., 2003), while on interdecadal timescales the North Atlantic climate exerts strong control on P_w, as indicated by the high negative correlations between P_w with the winter (December – March) North Atlantic Oscillation (wNAO) index (Styllas et al, 2016).

2.2 Glacial geomorphology

One of the most prominent features of Mount Olympus topography known to humans since antiquity, is the east facing Throne of Zeus cirque (TZ), escarped under the 150m high rock cliff of Stefani (meaning the crown in *Greek*, Fig. 3). Two well-preserved moraines (TZ-A, TZ-B), situated nearly perpendicular to each other, rest at an elevation of 2580m, bounding a surface area of 0.150 km^2 between the rock cliff base and the moraine crests (Fig. 3). TZ-A is a 2-4m high frontal moraine with an N-S orientation, parallel to the cliff base, located above a rock step. Below moraine TZ-A, the 30m high exposed rock step is indicative of a previous, likely a LGM glacier retreat, based on direct observations of glacial striations. Moraine TZ-A is morphostatigraphically overlain by a series of periglacial deposits and also by moraine TZ-B, an E-W oriented moraine with a 5-8m high well-developed crest. The periglacial deposits overlying moraine TZ-A include protalus ramparts, talus slope deposits and rockfall talus deposits, while below the characteristic rock band that separates the upper scree field with the underlying solifluction lobes, fresh talus deposited in the form of debris fans, are indicative of the high rates of the cliff discharging ability and sediment mobilization (Fig. 3). These periglacial deposits overlying moraine TZ-A in a stratigraphic upward sequence (Fig. 3 and 6A), suggest that the high supply rates of rock material, were likely forced by a change of the climate conditions from glacial to periglacial after the stabilization of TZ-A, however the timing remains unknown. In this east facing setting, direct inputs of solar insolation and high temperature differences between day and night are considered the main driving mechanisms for the observed high rates of physical weathering and the resultant high amounts of debris. The intense frost shattering leads to a continuous renewal of the cliff surface, thus the possibility of dating boulders with significant prior exposure from the cliff above is extremely low (Putkonen and Swanson, 2003).

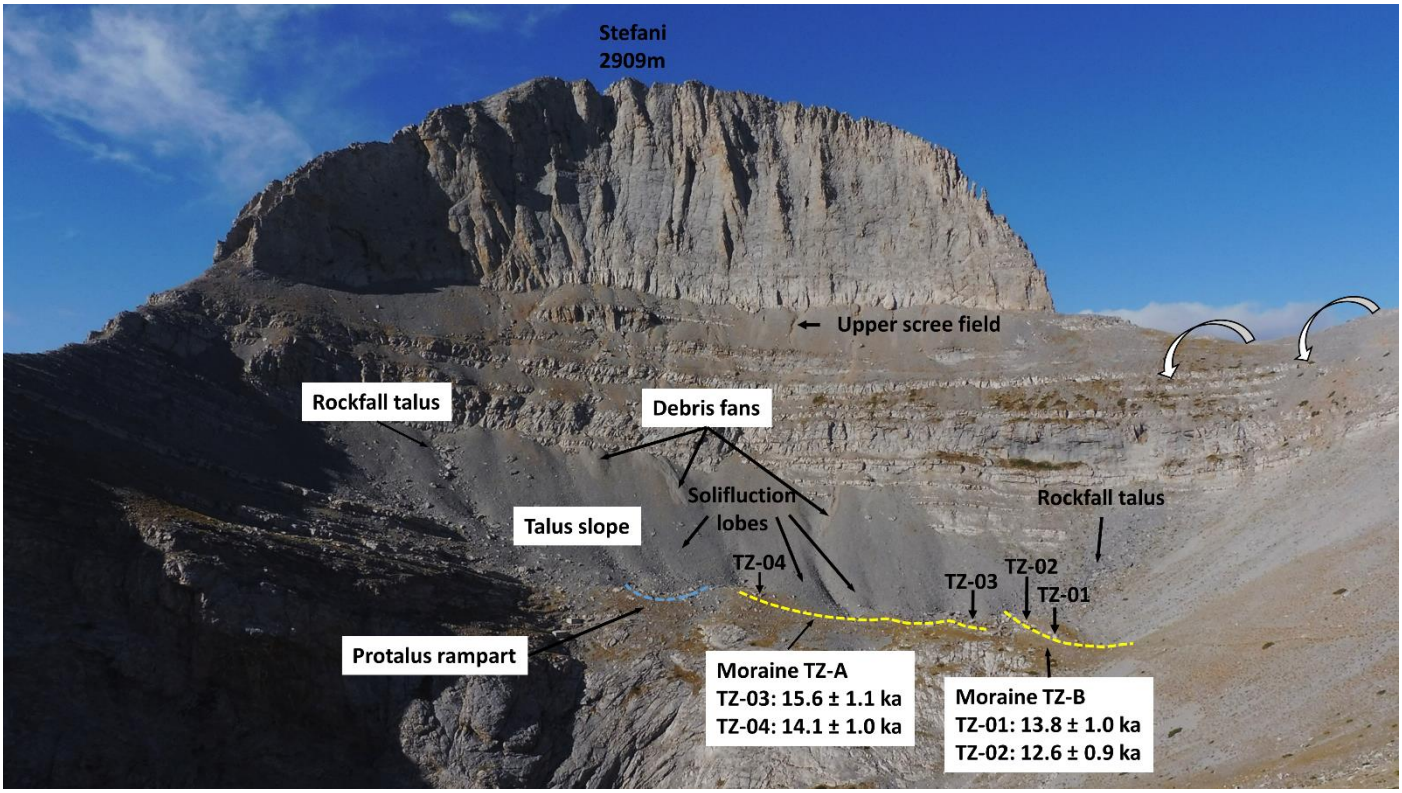

Fig. 3. The east facing Throne of Zeus (TZ) cirque with the 150m high headwall of Stefani (2909m). Moraines TZ-A and TZ-B are highlighted in yellow color. The locations and ages of the sampled boulders (#TZ-01–03) and bedrock (# TZ-04) are shown, with analytical errors only, and with the main periglacial features. The white curved arrows denote the direction of windblown and avalanching snow entering the cirque from the saddle above moraine TZ-B under W, SW and/or NW winds (direct observations).

The largest glacial landform of Mount Olympus and of Greece in general, is the NW-oriented head-valley cirque of Megala Kazania (MK), bounded by Mount Olympus highest peaks (Fig. 4). The cirque floor hosts three well-preserved groups of moraines (MK-A, MK-B and MK-C). Moraine group MK-A being located farthest from the cirque headwall, i.e. it is the oldest, and MK-C is the nearest, thus youngest moraine complex in the sequence (Styllas et al., 2016; Figs 2, 5). The cirque area between frontal moraine MK-A and the cirque headwall, is 0.5 km^2. MK-A (2155m) is overlain by an undated soil horizon (Sa) and fan-type glaciofluvial (Gf) deposits (Fig. 4). MK-B is bounded by the most characteristic and well-preserved moraine found on Mount Olympus (MK-B1, crest elevation 2225m; Fig. 5), a 65m-high frontal moraine with a steep distal slope (Fig. 4), inbound of which several other soil horizons are observed. Upslope of MK-B1, a variety of glacial landforms (multiple moraine crests, sinkholes, block accumulations, polished rock and striated surfaces) point to multiple episodes of glaciation (Figs 4 and 5), while in the downslope direction, MK-B1 is dissected by MK-B2 (Figs 4, 5, 8), which we tentatively interpreted as a push moraine; a landform interpreted by Smith et al. (1997) as a protalus rampart, during their field reconnaissance. Such talus-derived landforms have been associated with periglacial conditions and the formation of rock glaciers (Shakesby et al., 1987). However, the distinction between relict pronival-protalus ramparts and push moraines in the Alpine realm is not clear and the morphogenetic boundaries between the two often overlap (Scapozza, 2015), but here, we consider MK-B2 a push moraine, as we did not find additional evidence for the existence of an active rock glacier.

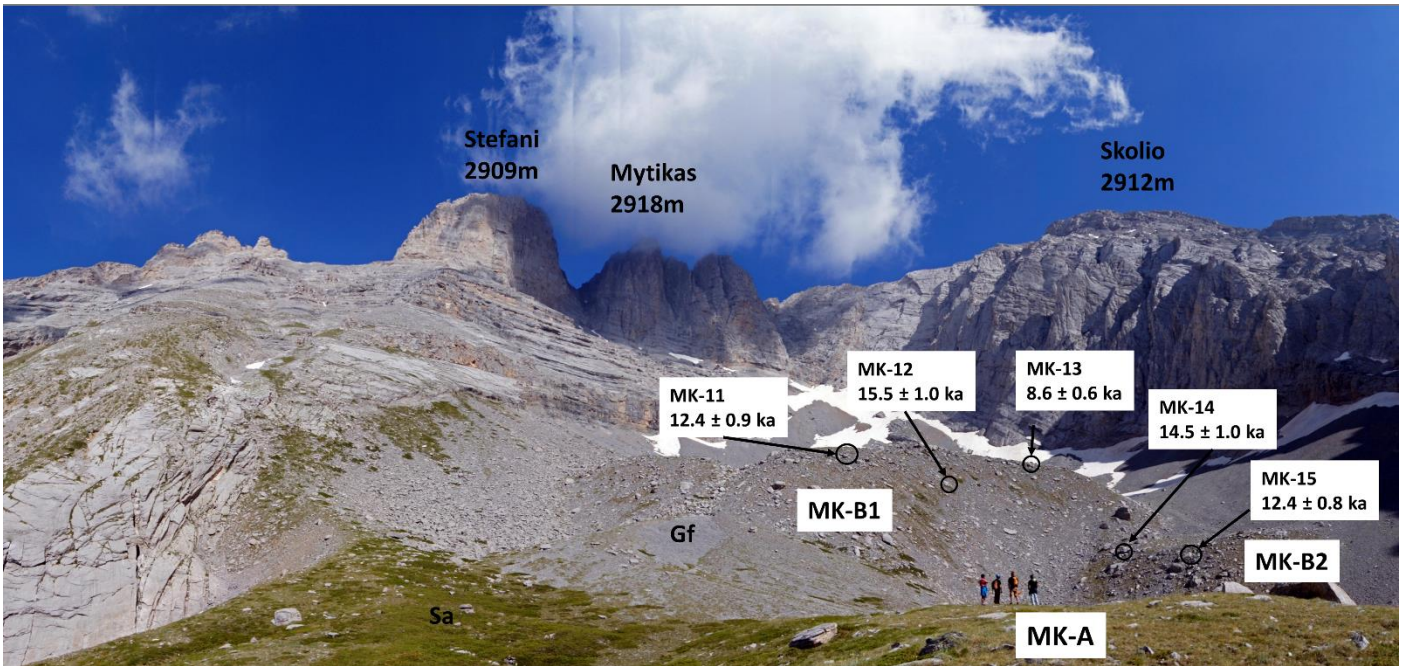

Fig. 4. Panoramic view of Megala Kazania (MK) cirque, with the most characteristic moraine MK-B1 in the foreground and Mount Olympus highest peaks and perennial snowfields in the background. The photograph is taken from morainic complex MK-A (white dot in Fig. 5), with the people standing on its crest. MK-A is stratigraphically overlain by the soil horizon Sa (with the grass cover) and by the 65m high moraine MK-B1, breached along its lateral sides by gravely glaciofluvial deposits (Gf) and by the push moraine MK-B2. The locations and ages of the sampled boulders # MK-11–15 are also shown, with analytical errors only.

Stratigraphically inboard of moraine MK-B1, two main glacial landforms are present: an apron of angular and sub-angular large block deposits (block sizes >0.5m), with a high degree of fragmentation and a series of transversal and longitudinal short and 5-7m high crests, sinkholes and near conical mounds of debris (Fig. 5). The transversal crest MK-B4 (2235m) and longitudinal crest MK-B5 (2245m), both of minimal curvature (Fig. 5, 8, 9A and 9B) and located closer to the cirque center than moraine MK-B3, are interpreted as a set of hummocky moraines. Behind these landforms and closer to the cirque walls, a series of blocky moraines, ascribed to morainic complex MK-C. MK-C group of moraines are 2 – 4m high and less developed compared to MK-B moraine crests (Fig. 5), suggesting shorter periods of glacier-friendly climatic conditions and moraine stabilization. Blocky moraines MK-C1 – 2240m, MK-C2 – 2290m, MK-C3 – 2250m and MK-C4 – 2270m, are either nested within older MK-B moraines (as for example moraine MK-C1 is nested in moraine MK-B3 – 2240m; Fig. 5), or breached by glaciofluvial activity (MK-C2), or located higher up and very close to the cirque walls (MK-C4), where extant snowfields still survive (Fig. 5). Inboard (upvalley) of moraine MK-C3, isolated boulders deposited along a longitudinal ridge parallel to the cirque centerline, are interpreted as supraglacial deposition during the latter stages of MK glacial activity. In contrast to the color of the MK-B deposits, the boulders of moraine complex MK-C are characterized by darker color and show no degree of fragmentation (Fig. 5).

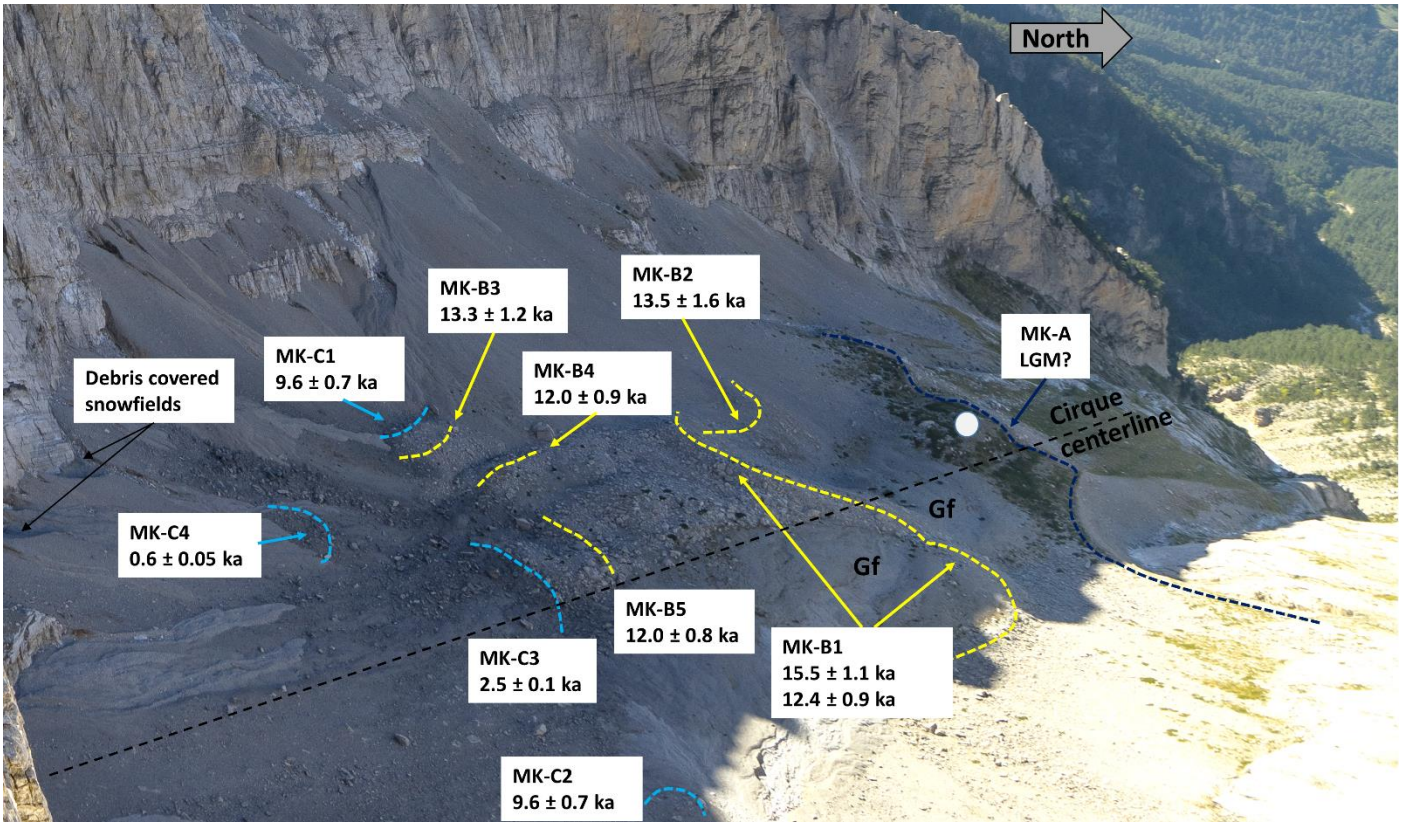

Fig. 5. The view of Megala Kazania (MK) cirque from the summit of Mount Olympus, Mytikas (2918m). The photograph was taken on October 1st 2016, at the beginning of the snow accumulation season, when debris-covered extant snowfields still survive in the shaded parts of the cirque below the steep cliffs of Skolio (2912m). Moraine complexes MK-A (dark blue dashed line), MK-B (yellow dashed lines) and MK-C (light blue dashed lines) and sampled moraine crests (MK-B1–B5, MK-C1-C4) are shown with their respective ^{36}Cl ages, either based on a single sample, or on the arithmetic mean of two or three samples were available. For intersite comparisons between the various landforms of TZ and MK cirques, we do not include the production rate errors in the age uncertainties shown here. Outwash plain glaciofluvial deposits (Gf) that breach the (north) right side of moraine MK-B1 along the cirque centerline, and the boulder apron bounded between hummocky moraines MK-B4, MK-B5 and frontal moraine MK-B1, are also illustrated. The white dot represents the location, where the people are standing in Fig. 4.

3. *In situ*-produced ^{36}Cl-based cosmic ray exposure dating of Throne of Zeus (TZ) and Megala Kazania (MK) moraines

3.1 Fieldwork and collection of samples

During summer and fall of 2015 and 2016, a fieldwork reconnaissance took place and initially involved the detailed mapping of all glacial features (moraines, striated bedrock and glacial sediments) in both cirques. In addition to the mapping of the moraines, we collected 20 samples (16 samples from MK and 4 samples from TZ, Fig. 2, and Table 1). One sample was retrieved from bedrock (sample TZ-04) and the other 19 samples from glacially transported boulders.

Table 1
Geographical characteristics, boulder heights and topographic shielding and snow cover correction factors for the ^{36}Cl-dated samples

Sample & Landform ID	Latitude ºN (DD) WGS 84	Longitude ºE (DD) WGS 84	Landform Elevation (m)	Boulder height (m)	Shielding Factor	Snow correction factor	Boulder location
Moraine TZ-A			**2592**			0.94	
TZ-03	40.0910	22.3609	2597	0.75	0.931		Moraine crest
TZ-04	40.0903	22.3612	2585	1.25	0.931		Bedrock inboard of moraine

Moraine TZ-B			**2580**			0.94	
TZ-01	40.0912	23.3608	2587	1.0	0.932		Moraine crest
TZ-02	40.0911	23.3608	2575	0.6	0.946		Moraine crest
Moraine MK-B1			**2225**			0.94	
MK-11	40.0889	22.3487	2220	0.6	0.894		Embedded on outer slope below moraine crest
MK-12	40.0885	22.3483	2215	0.5	0.902		Embedded on outer slope below moraine crest
MK-13	40.0887	22.3486	2223	0.7	0.906		Deposited on outer slope below moraine crest
Moraine MK-B2			**2175**			0.94	
MK-14	40.0890	22.3476	2170	1.2	0.871		Embedded in protalus rampart
MK-15	40.0891	22.3474	2167	0.9	0.884		Embedded in protalus rampart
Moraine MK-B3			**2240**			0.90	
MK-03	40.0872	22.3489	2235	0.6	0.820		Embedded in moraine crest
MK-05	40.0873	22.3487	2240	0.7	0.844		Top of moraine crest
Moraine MK-B4			**2245**			0.94	
MK-10	40.0874	22.3489	2245	0.9	0.852		Top of hummocky moraine
Moraine MK-B5			**2245**				
MK-07	40.0878	22.3498	2245	0.4	0.881		Top of hummocky moraine
Moraine MK-C1			**2240**			0.94	
MK-02	40.0874	22.3501	2238	2.0	0.864		Inbound of moraine crest
MK-02a	40.0874	22.3500	2236	1.5	0.864		Inbound of moraine crest
MK-06	40.0874	22.3496	2236	0.3	0.852		Embedded in outer slope of moraine
Moraine MK-C2			**2290**			0.90	
MK-04	40.0871	22.3486	2290	0.9	0.821		Crest top of moraine MK-C2, nested in MK-B3
Moraine MK-C3			**2250**			0.90	
MK-09	40.0864	22.3501	2250	1.1	0.818		On top of blocky moraine
Moraine MK-C4			**2300**			0.90	
MK-01	40.0876	22.3522	2300	1.8	0.848		On top of breached lateral moraine
MK-01a	40.0876	22.3520	2300	3.0	0.848		On top of breached lateral moraine

* MK: Megala Kazania cirque, TZ: Throne of Zeus cirque

The samples from the TZ and MK cirques were retrieved using a hammer and a chisel from flat or slightly tilted surfaces of selected limestone boulders that were either embedded or rested on the top of eleven moraine crests (TZ-A–B, MK-B1–B5 and MK-C1–C4, Fig. 2, 3 and 4). Their coordinates were logged in a hand-held GPS (Garmin E-trex). Boulders with evidence of post depositional movement (toppling) were avoided as were boulder surfaces with high degree of fragmentation and signs of surface and rill erosion. The boulders' heights, landform elevations and the surrounding topographic shieldings are given in Table 1.

3.2 Sample preparation and exposure ages calculations

The samples were physically and chemically prepared at the Centre Européen de Recherche et d' Enseignement des Geosciences de l'Environnement (CEREGE) in Aix en Provence, France, following

standard procedures (modified from Stone et al., 1996; Schlagenhauf et al., 2010). After mechanical crushing and sieving of the 20 samples, ~35 g of the 0.25–0.5mm grain size fractions were first washed in H_2O and then leached in 2M HNO_3 in order to remove atmospheric and potential secondary Cl. After total dissolution of the leached grains in 2M HNO_3, a ^{35}Cl-enriched spike solution containing ~1.9 mg Cl was added to the sample solutions. From this step on, two chemistry blanks were processed, one for each batch of 10 samples. The solutions were filtered to remove any solid residues. From these solutions, an 1 ml aliquot was taken to later conduct measurements of the Ca concentrations in the dissolved samples by inductive coupled plasma atomic emission spectrometry (ICP-AES) at CEREGE (Table 2). 2 ml of a 10% $AgNO_3$ solution were added to the remaining filtered solutions to precipitate AgCl, and after two days the supernatant was removed by pumping and centrifuging. After re-dissolving the AgCl in NH_3aq, the removal of S from the solution was achieved through addition of 0.5 ml of a saturated $Ba(NO_3)_2$ solution, which resulted in precipitation of $BaSO_4$. The remaining solutions were filtered with syringes through 0.45µm-mesh filters, and AgCl was re-precipitated by adding ~2 ml of concentrated HNO_3. The rinsed and dried AgCl pellets were pressed into nickel cathodes and measured by isotope dilution accelerator mass spectrometry (AMS) (Bouchez et al. 2015, Ivy-Ochs et al., 2004) at French AMS national facility ASTER at CEREGE (Arnold et al., 2013). Both the $^{36}Cl/^{35}Cl$ and the $^{35}Cl/^{37}Cl$ ratios were obtained by normalization to inhouse standard SM-CL-12 with an assigned $^{36}Cl/^{35}Cl$ value of $(1.428 \pm 0.021) \times 10^{-12}$ (Merchel et al., 2011), and assuming a natural $^{35}Cl/^{37}Cl$ ratio of 3.127. From these measured ratios, the samples' ^{36}Cl and Cl concentrations were calculated (Table 2).

The ^{36}Cl ages were calculated using the Excel® spreadsheet published in Schimmelpfennig et al. (2009), using the ^{36}Cl production rate for spallation of Ca, referenced to sea level and high latitude (SLHL), of 42.2 ± 4.8 atoms ^{36}Cl $(g\ Ca)^{-1}\ yr^{-1}$ (Schimmelpfennig et al., 2011) with the time-invariant scaling method by Stone (2000). This SLHL ^{36}Cl production rate for spallation of Ca was calibrated with Ca-rich feldspars from lava surface samples collected at Mount Etna volcano, which is the closest to Mt Olympus among all currently existing ^{36}Cl calibration sites. In addition, its value is supported by the SLHL ^{36}Cl spallation production rate inferred from fitting modelled ^{36}Cl data to ^{36}Cl measurements from a calcium carbonate depth profile in south-eastern France (Braucher et al., 2011). The production rate of epithermal neutrons from fast neutrons in the atmosphere at the land/atmosphere interface of 696 ± 185 neutrons $(g\ air)^{-1}\ yr^{-1}$ for (Marrero et al., 2016) was applied. Due to the low Cl concentrations in these limestones (5-23 ppm), the contribution of ^{36}Cl production from low-energy-neutron capture by ^{35}Cl accounts for only between 1% and 6% of the total ^{36}Cl production. A high-energy neutron attenuation length of 160 g cm^{-2} was used. We assumed a bulk rock density of 2.7 g cm^{-3} for all samples. Age uncertainties correspond to 1σ; in Table 3 we show the full uncertainties in the individual ages (both analytical and production rate errors are propagated through) as well as the analytical uncertainties only. For the moraines that contain more than one dated boulder, we tested the consistency of the ages through the χ^2 criterion (Ward and Wilson, 1978, outliers are shown in Table 3) and we then calculated the arithmetic mean to obtain the moraine age (Table 3, Fig. 7). Unless otherwise stated, the uncertainties in the mean moraine ages include the standard deviation and the analytical and production rate errors added by propagation in quadrature.

3.3 Corrections for snow and denudation

The calculated SED ages were corrected for snow cover, which is not temporally uniform among the landforms under consideration, according to our modern yearly observations. The studied moraines were therefore divided into two groups. Group 1 comprises moraines MK-B3, -C1, -C2 and -C4 (Fig. 5), which are situated close to the high MK cirque cliffs and are affected by the pronounced effects of windblown and avalanching snow from the cliffs above; they are snow-covered for ~7 months per year. Group 2 includes moraines TZ-A, -B and moraines MK-B1,-B4, -B5, -C3 and push moraine / protalus rampart MK-B2, which are distant from the MK cirque cliffs and are exposed ~2 months earlier during the snowmelt season than the moraines of group 1. It has to be noted that correcting cosmogenic nuclide production rates for the effect of snow cover is challenging for two reasons. First, the exact quantity and yearly duration of snow cover during the period of exposure of the rock surface is generally not known; and second, it is still debated how to correctly model the effect of snow on the different production reactions of the various cosmogenic nuclides, in particular those of multi-reaction-produced ^{36}Cl (Masarik et al., 2007; Zweck et al., 2013; Dunai et al., 2014; Delunel et al., 2014).

As the ^{36}Cl in our samples is dominantly produced by spallation of Ca, we approximate snow correction factors for both above-mentioned moraine groups in a first step, based on the classical equation for the effect

of snow cover by Gosse and Phillips (2001), which assumes that the snow pack shields the rock surface and therefore reduces the spallogenic cosmogenic nuclide production compared to no-snow-conditions. For this calculation, we consider a snow pack of 2 m with a snow density of 0.2 g cm^{-3} for 7 and 5 months for moraine groups 1 and 2, respectively. However, we suspect that the snow correction factors of 0.87 and 0.91 resulting from these estimates might overestimate the impact of snow, because the slight presence of ^{35}Cl in our samples (section 3.2) results in the opposite of the shielding effect on the spallogenically produced ^{36}Cl; i.e. hydrogen in snow enhances the low-energy neutron flux at the air/rock interface and thus increases the ^{36}Cl surface production from low-energy-neutron capture by ^{35}Cl (Masarik et al., 2007; Zweck et al., 2013; Dunai et al., 2013). In a second step, we therefore estimate a related ^{36}Cl production increase of 3%, approximated from the correction factors proposed in Fig. 7 of Dunai et al. (2014), resulting in total snow correction factors of 0.90 for moraine group 1 and 0.94 for moraine group 2, i.e. the ^{36}Cl production is reduced by 10% and 6%, respectively, compared to no-snow-conditions.

In the lack of quantitative estimates for denudation of the calcareous rock formations in the southern Balkan region and taking into account the fact that the sampled boulders showed minimal signs of surface and/or rill erosion, we discuss our ^{36}Cl ages without any correction for denudation. These therefore correspond to minimum exposure ages. However, in Table 3 we also provide the ^{36}Cl ages including a denudation rate of 5mm/ka, as this value was applied in the calculation of ^{36}Cl moraine ages in a recent study from the Balkan region (Gromig et al., 2017). Anyway, the exposure ages calculated both ways for all samples are not significantly different taking into account the associated uncertainties.

Table 2. Chemical data and AMS measurement results.

Sample & Landform ID	Sample weight (g)	ASTER cathode	Mass of Cl in spike (mg)	$^{35}Cl/^{37}Cl$	$^{36}Cl/^{35}Cl$ (10^{-13})	Cl concentration (ppm)	^{36}Cl blank correction	^{36}Cl concentration (10^5 atoms g^{-1})	CaO concentrations (%)
Moraine TZ-A									
TZ-03	36.28	BVOY	1.893	17.94 ± 0.24	14.79 ± 0.53	13.85 ± 0.23	0.28%	15.98 ± 0.58	53.87 ± 0.64
TZ-04 (bedrock)	35.74	BVON	1.585	10.596 ± 0.099	13.92 ± 0.48	23.30 ± 0.32	0.23%	14.97 ± 0.52	53.59 ± 0.58
Moraine TZ-B									
TZ-01	35.94	BVOX	1.891	29.8 ± 0.52	14.36 ± 0.50	7.38 ± 0.16	0.31%	14.42 ± 0.51	54.70 ± 0.62
TZ-02	35.05	BVOM	1.833	16.93 ± 0.24	11.99 ± 0.42	14.30 ± 0.27	0.27%	13.15 ± 0.46	52.85 ± 0.53
Moraine MK-B1									
MK-11	33.44	BVOT	1.872	31.17 ± 0.66	10.03 ± 0.40	7.43 ± 0.20	0.45%	10.65 ± 0.43	56.73 ± 0.68
MK-12	35.30	BVOU	1.870	23.11 ± 0.38	9.64 ± 0.33	10.20 ± 0.21	0.45%	10.09 ± 0.35	44.03 ± 0.45
MK-13 (*outlier*)	34.68	BVOV	1.886	26.44 ± 0.38	6.76 ± 0.27	8.21 ± 0.16	0.50%	7.11 ± 0.29	55.68 ± 0.78
Moraine MK-B2									
MK-14	34.80	BVOW	1.810	24.99 ± 0.36	11.03 ± 0.39	9.07 ± 0.17	0.41%	11.19 ± 0.39	55.77 ± 0.56
MK-15	35.42	BVOJ	1.886	40.88 ± 0.49	9.66 ± 0.33	5.038 ± 0.084	0.47%	9.51 ± 0.33	55.51 ± 0.60
Moraine MK-B3									
MK-03	34.37	BVOQ	1.827	30.07 ± 0.59	8.88 ± 0.36	7.36 ± 0.18	0.52%	8.99 ± 0. 36	55.88 ± 0.63
MK-05	35.00	BVOS	1.870	27.02 ± 0.31	10.05 ± 0.40	8.47 ± 0.12	0.44%	10.37 ± 0.41	55.09 ± 0.63
Moraine MK-B4									
MK-10	32.85	BVOI	1.903	23.87 ± 0.32	8.39 ± 0.35	10.04 ± 0.18	0.39%	9.55 ± 0.40	54.90 ± 0.61
Moraine MK-B5									
MK-07	35.66	BVOG	1.902	25.70 ± 0.35	8.97 ± 0.21	8.37 ± 0.15	0.37%	9.30 ± 0.22	53.36 ± 0.66
Moraine MK-C1									
MK-04	35.26	BVOR	1.844	35.85 ± 0.57	6.95 ± 0.29	5.82 ± 0.12	0.67%	6.78 ± 0.28	55.24 ± 0.71
Moraine MK-C2									
MK-01	35.09	BVOP	1.852	24.86 ± 0.42	7.24 ± 0.31	9.27 ± 0.20	0.61%	7.45 ± 0.32	55.90 ± 0.63
MK-01a (*outlier*)	36.72	BVOK	1.859	22.36 ± 0.32	12.71 ± 0.44	9.55 ± 0.18	0.26%	12.79 ± 0.45	54.80 ± 0.54
Moraine MK-C3									
MK-02	35.49	BVOE	1.814	36.30 ± 0.51	2.144 ± 0.063	4.954 ± 0.099	1.69%	2.021 ± 0.061	53.38 ± 0.78
MK-02a	33.54	BVOL	1.872	38.1 ± 1.1	2.074 ± 0.089	5.08 ± 0.21	1.71%	2.125 ± 0.093	57.66 ± 0.69
MK-06	34.04	BVOF	1.897	30.26 ± 1.1	1.736 ± 0.091	7.018 ± 0.35	1.96%	1.81 ± 0.10	54.87 ± 0.67
Moraine MK-C4									
MK-09	31.06	BVOH	1.898	26.18 ± 0.37	0.431 ± 0.023	9.36 ± 0.17	7.76%	0.473 ± 0.030	54.95 ± 0.57

					Total number of Cl atoms (10^{15})	Total number of ^{36}Cl atoms (10^{3})
blanc Hera	BVOO	1.882	267 ± 11	0.049 ± 0.011	359 ± 21	160 ± 36
blanc Athena	BVOD	1.812	148.6 ± 2.0	0.039 ± 0.011	741 ± 12	124 ± 35

Table 3. Individual ^{36}Cl sample and landform ages of Throne of Zeus (TZ) and Megala Kazania (MK) cirques. Ages are shown without denudation and snow correction as well as corrected with the snow correction factors of Table 1 and/or for a denudation rate of 5mm/ka. Please note that the ages only corrected for snow cover are those discussed in the text (see text for details). All uncertainties are reported at 1σ level. Uncertainties in the individual ages include the analytical and production rate errors, while italic numbers in parentheses are the analytical errors only. Uncertainties in the mean moraine ages include the standard deviation, analytical and production rate errors, while italic numbers in parentheses are the standard deviations only. Outlier samples are shown in italics.

No correction		**Snow correction only**		**Erosion correction (5mm/ka)**		**Snow correction & erosion correction (5mm/ka)**	
Sample & Landform ID	**Age (ka)**	**Sample & Landform ID**	**Age (ka)**	**Sample & Landform ID**	**Age (ka)**	**Sample & Landform ID**	**Age (ka)**
TZ-A	**14.13 ± 2.03** ***(0.99)***	**TZ-A**	**14.86 ± 2.15** ***(1.08)***	**TZ-A**	**14.58 ± 2.19** ***(1.20)***	**TZ-A**	**15.42 ± 2.33** ***(1.31)***
TZ-03	14.83 ± 1.88 *(1.04)*	TZ-03	15.62 ± 1.97 *(1.10)*	TZ-03	15.44 ± 1.95 *(1.09)*	TZ-03	16.35 ± 2.06 *(1.15)*
TZ-04	13.43 ± 1.67 *(0.93)*	TZ-04	14.09 ± 1.74 *(0.97)*	TZ-04	13.73 ± 1.71 *(0.95)*	TZ-04	14.50 ± 1.80 *(1.00)*
TZ-B	**12.54 ± 1.76** ***(0.75)***	**TZ-B**	**13.23 ± 1.86** ***(0.82)***	**TZ-B**	**13.02 ± 1.88** ***(0.91)***	**TZ-B**	**13.80 ± 2.00** ***(1.00)***
TZ-01	13.07 ± 1.67 *(0.91)*	TZ-01	13.82 ± 1.76 *(0.97)*	TZ-01	13.66 ± 1.76 *(0.96)*	TZ-01	14.50 ± 1.85 *(1.02)*
TZ-02	12.01 ± 1.51 *(0.83)*	TZ-02	12.65 ± 1.58 *(0.88)*	TZ-02	12.37 ± 1.56 *(0.86)*	TZ-02	13.10 ± 1.64 *(0.91)*
MK-B1	**13.21 ± 2.67** ***(2.09)***	**MK-B1**	**13.94 ± 2.80** ***(2.19)***	**MK-B1**	**13.75 ± 2.80** ***(2.20)***	**MK-B1**	**14.58 ± 2.95** ***(2.31)***
MK-11	11.73 ± 1.47 *(0.85)*	MK-11	12.39 ± 1.54 *(0.90)*	MK-11	12.20 ± 1.52 *(0.88)*	MK-11	12.94 ± 1.61 *(0.94)*
MK-12	14.69 ± 1.86 *(1.02)*	MK-12	15.49 ± 1.95 *(1.08)*	MK-12	15.31 ± 1.93 *(1.06)*	MK-12	16.22 ± 2.04 *(1.13)*
MK-13	*8.13 ± 1.04 (0.59)*	*MK-13*	*8.58 ± 1.10 (0.62)*	*MK-13*	*8.33 ± 1.07 (0.60)*	*MK-13*	*8.83 ± 1.13 (0.64)*
MK-B2	**12.77 ± 2.17** ***(1.44)***	**MK-B2**	**13.49 ± 2.28** ***(1.51)***	**MK-B2**	**13.32 ± 2.27** ***(1.52)***	**MK-B2**	**14.13 ± 2.40** ***(1.60)***
MK-14	13.79 ± 1.75 *(0.96)*	MK-14	14.56 ± 1.84 *(1.01)*	MK-14	14.40 ± 1.83 *(1.00)*	MK-14	15.27 ± 1.93 *(1.06)*
MK-15	11.75 ± 1.50 *(0.81)*	MK-15	12.42 ± 1.58 *(0.86)*	MK-15	12.25 ± 1.56 *(0.85)*	MK-15	13.00 ± 1.65 *(0.90)*
MK-B3	**12.12 ± 1.90** ***(1.09)***	**MK-B3**	**13.32 ± 2.09** ***(1.20)***	**MK-B3**	**12.60 ± 2.00** ***(1.17)***	**MK-B3**	**13.92 ± 2.21** ***(1.31)***
MK-03	11.34 ± 1.46 *(0.82)*	MK-03	12.47 ± 1.60 *(0.90)*	MK-03	11.77 ± 1.51 *(0.85)*	MK-03	13.00 ± 1.66 *(0.94)*
MK-05	12.89 ± 1.66 *(0.93)*	MK-05	14.17 ± 1.81 *(1.02)*	MK-05	13.43 ± 1.72 *(0,97)*	MK-05	14.85 ± 1.90 *(1.07)*
MK-B4	**11.33 ± 1.42** ***(0.83)***	**MK-B4**	**11.97 ± 1.50** ***(0.90)***	**MK-B4**	**11.73 ± 1.47** ***(0.86)***	**MK-B4**	**12.43 ± 1.56** ***(0.92)***
MK-10	11.33 ± 1.42 *(0.83)*	MK-10	11.97 ± 1.50 *(0.90)*	MK-10	11.73 ± 1.47 *(0.86)*	MK-10	12.43 ± 1.56 *(0.92)*
MK-B5	**11.42 ± 1.42** ***(0.74)***	**MK-B5**	**12.06 ± 1.49** ***(0.78)***	**MK-B5**	**11.84 ± 1.47** ***(0.76)***	**MK-B5**	**12.55 ± 1.55** ***(0.81)***
MK-07	11.42 ± 1.42 *(0.74)*	MK-07	12.06 ± 1.49 *(0.78)*	MK-07	11.84 ± 1.47 *(0.76)*	MK-07	12.55 ± 1.55 *(0.81)*
MK-C1	**8.77 ± 1.13** ***(0.64)***	**MK-C1**	**9.64 ± 1.24** ***(0.71)***	**MK-C1**	**9.03 ± 1.16** ***(0.66)***	**MK-C1**	**9.97 ± 1.28** ***(0.73)***
MK-04	8.77 ± 1.13 *(0.64)*	MK-04	9.64 ± 1.24 *(0.71)*	MK-04	9.03 ± 1.16 *(0.66)*	MK-04	9.97 ± 1.28 *(0.73)*

MK-C2	**8.76 ± 1.13 *(0.64)***	**MK-C2**	**9.61 ± 1.23 *(0.71)***	**MK-C2**	**9.00 ± 1.16 *(0.66)***	**MK-C2**	**9.91 ± 1.27 *(0.73)***
MK-01	8.76 ± 1.13 *(0.64)*	MK-01	9.61 ± 1.23 *(0.74)*	MK-01	9.00 ± 1.16 *(0.66)*	MK-01	9.91 ± 1.27 *(0.73)*
MK-01a	*15.30 ± 1.95 (1.06)*	*MK-01a*	*16.81 ± 2.13 (1.17)*	*MK-01a*	*16.05 ± 2.03 (1.12)*	*MK-01a*	*17.75 ± 2.25 (1.24)*
MK-C3	**2.37 ± 0.32 *(0.12)***	**MK-C3**	**2.51 ± 0.34 *(0.13)***	**MK-C3**	**2.39 ± 0.33 *(0.12)***	**MK-C3**	**2.53 ± 0.35 *(0.13)***
MK-02	2.44 ± 0.30 *(0.16)*	MK-02	2.58 ± 0.32 *(0.17)*	MK-02	2.46 ± 0.31 *(0.16)*	MK-02	2.61 ± 0.32 *(0.17)*
MK-02a	2.44 ± 0.31 *(0.18)*	MK-02a	2.58 ± 0.33 *(0.19)*	MK-02a	2.46 ± 0.32 *(0.18)*	MK-02a	2.60 ± 0.33 *(0.19)*
MK-06	2.23 ± 0.29 *(0.18)*	MK-06	2.35 ± 0.31 *(0.19)*	MK-06	2.24 ± 0.30 *(0.18)*	MK-06	2.37 ± 0.31 *(0.19)*
MK-C4	**0.58 ± 0.08 *(0.05)***	**MK-C4**	**0.64 ± 0.09 *(0.05)***	**MK-C4**	**0.58 ± 0.08 *(0.05)***	**MK-C4**	**0.64 ± 0.09 *(0.05)***
MK-09	0.58 ± 0.08 *(0.05)*	MK-09	0.64 ± 0.09 *(0.05)*	MK-09	0.58 ± 0.08 *(0.05)*	MK-09	0.64 ± 0.09 *(0.05)*

4. Mount Olympus Late-glacial and Holocene glacial chronology

In the following text, we present the ^{36}Cl ages that are corrected for the snow shielding effect. For the sake of internal comparison between all ^{36}Cl ages, the individual ^{36}Cl ages in this section are presented with the analytical errors only and the mean ages are given as arithmetic means with their standard deviations (Table 3).

4.1 Throne of Zeus (TZ) cirque

The ^{36}Cl ages of the three boulders (TZ-01–03) and one bedrock sample (TZ-04) from TZ cirque, range between 15.6 ± 1.1 and 12.65 ± 0.88 ka (Table 3). Boulder sample TZ-03 (15.62 ± 1.1 ka) lies on the inner slope of frontal moraine TZ-A, 0.5m below its crest, while bedrock sample TZ-04 (14.08 ± 0.98 ka) was taken from a bench that outcrops along the inner side of TZ-A (Fig. 6C, D).

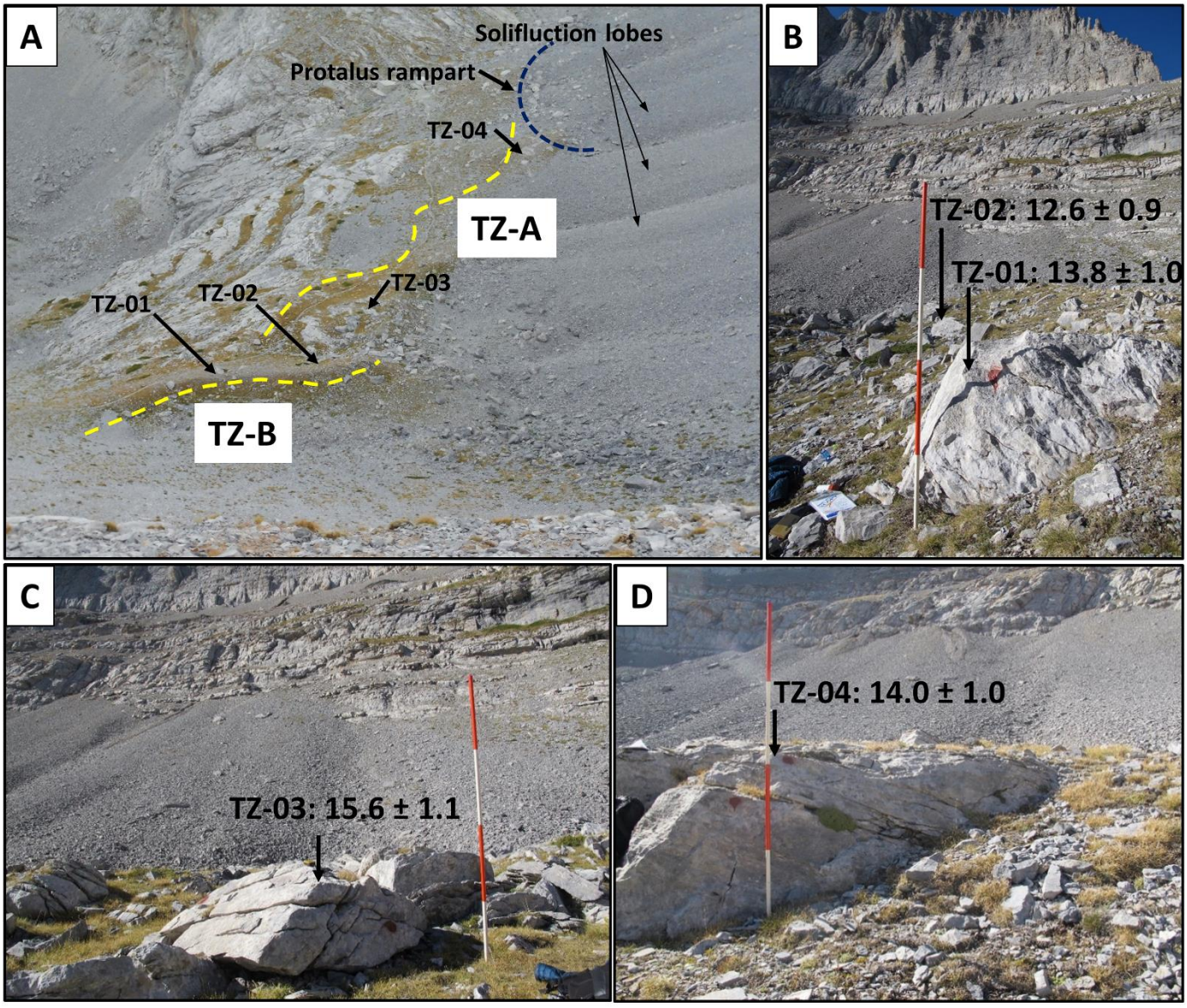

Fig. 6. A) General view of Throne of Zeus cirque frontal moraine TZ-A and lateral moraine TZ-B, together with the sampled boulders and bedrock. B, C, and D) Sampled boulders TZ-01 and TZ-02, TZ-03 and TZ-04, with their respective calculated ages including analytical errors only.

The individual ages of samples TZ-03 and TZ-04 were not tested against the χ^2 criterion, because the age of boulder sample TZ-03 is considered to correspond to the moment of stabilization of the moraine, while bedrock sample TZ-04 was most likely exposed during the subsequent glacier retreat, as suggested by the chronological order of their ^{36}Cl ages. Samples TZ-01 (13.82 ± 0.97 ka) and TZ-02 (12.65 ± 0.88 ka) were obtained from flat-top parts of embedded boulders located on the outer slope of moraine TZ-B, 2m below the well-defined crest (Fig. 6A, B). They give a mean age of 13.2 ± 1.9 ka (Fig. 7A). The stratigraphical

position of the geomorphologically distinct moraines TZ-A and TZ-B, imply a two-phase glacier behaviour of the TZ paleoglacier; a stabilization phase at 15.6 ± 1.1 ka that terminated around 14.0 ± 1.7 ka with the exposure of bedrock (sample TZ-04), and a subsequent re-advance or stagnation phase that resulted in the built-up and stabilization of moraine TZ-B at 13.2 ± 1.9 ka (Fig. 6A).

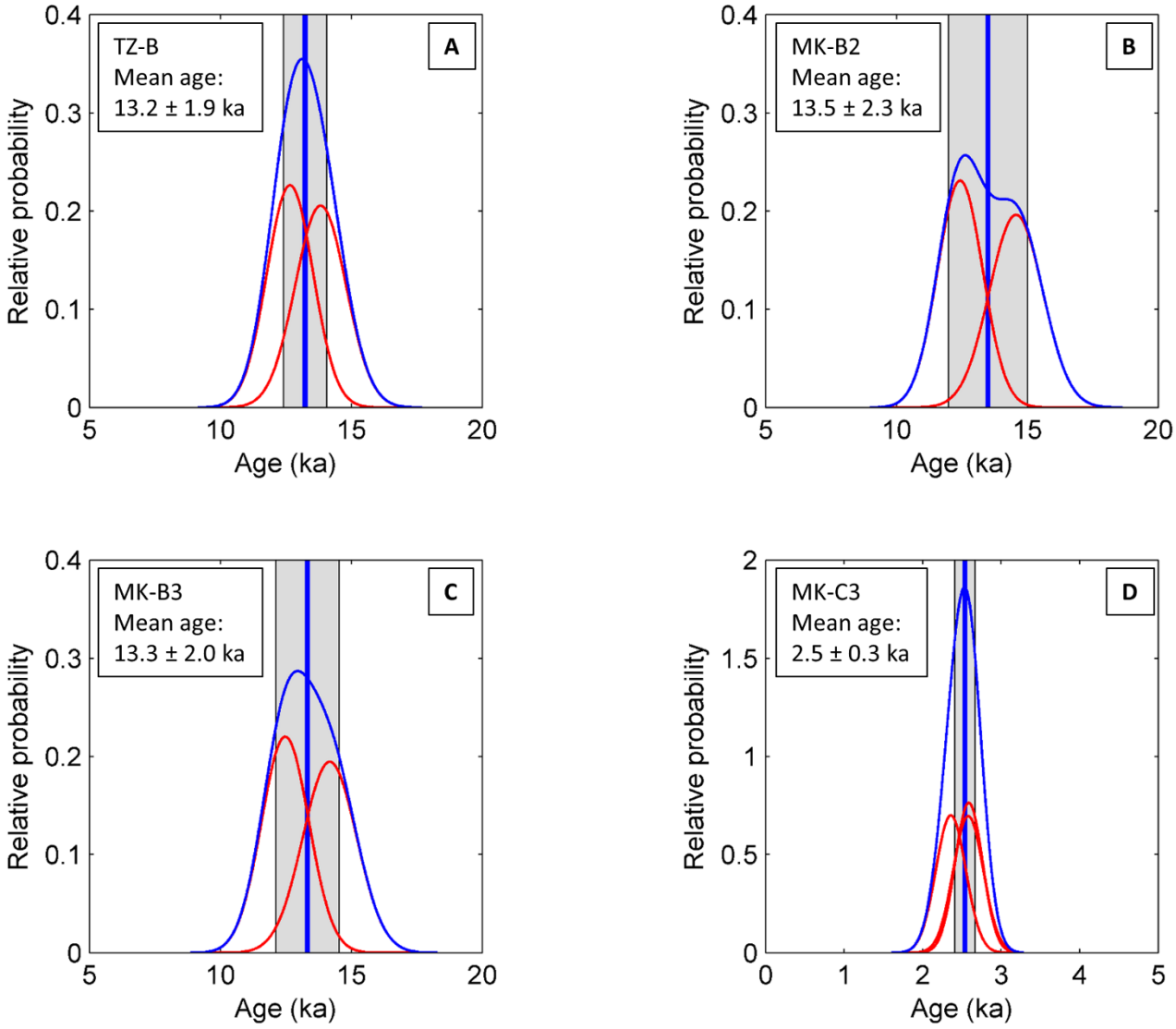

Fig. 7. Probability density function plots of the TZ and MK landforms (moraines and pronival rampart) with more than one ^{36}Cl age that comply with the χ^2 criterion test. Individual boulder ages (red Gaussian distributions) are shown with their analytical errors only. The landform age distribution is represented by the blue summary curve. Blue vertical lines and grey bands are the arithmetic means and standard deviations of the landform ages, while the arithmetic mean ages given in the upper left corner of each panel are shown with the full uncertainty (including standard deviation, analytical and production rate errors). Ages are corrected for snow cover.

Megala Kazania (MK) cirque

The sixteen (n=16) ^{36}Cl boulder ages sampled in MK cirque range from 15.5 ± 1.1 ka to 0.64 ± 0.05 ka (Table 3), spanning the Late-glacial and Holocene. Moraine MK-B1 is a composite feature as evident from several soil horizons observed on its outer slope and on the outwash plain on its inner slope (Fig. 4, 5 and 8). Boulders resting on the crest (yellow dashed line in Fig. 8) showed high degree of fragmentation and signs of block rotation and were therefore not suitable for sampling. Instead, three boulders (MK-11, MK-12, and MK-13) were sampled from different levels of the ~65 m high steep outer slope, i.e. 5m, 10m, and 2m below the crest, respectively (Fig. 4). Boulders MK-11 and MK-12 were in stable positions, embedded in the moraine's slope, thus minimizing the potential of block toppling from above, whereas boulder MK-13 was resting on the slope, in a rather instable position.

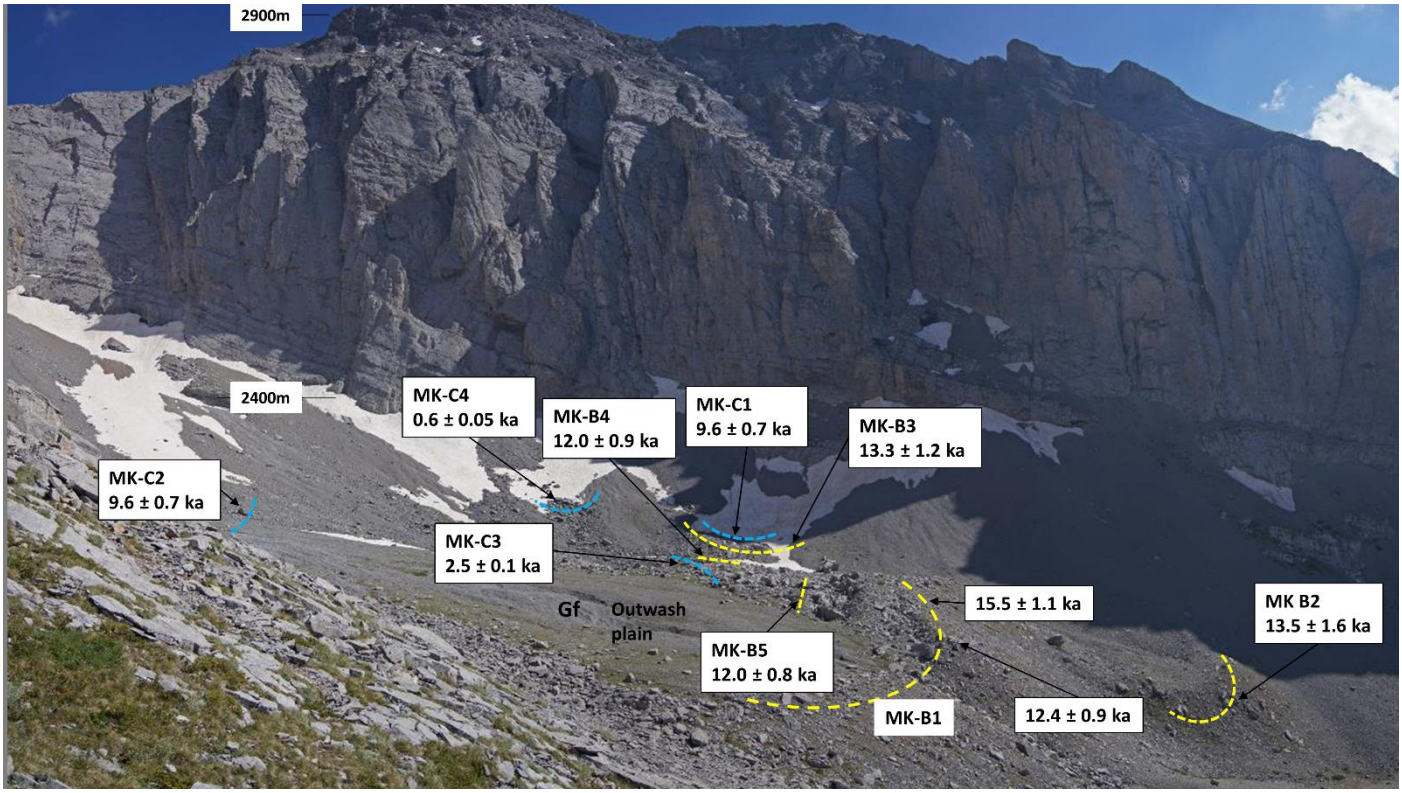

Fig. 8. A: Panoramic view of the Megala Kazania cirque, bounded by the 500m north wall of Skolio (2912m), together with the ages (analytical errors only) of moraines MK-B1, -B3, -B4, B5, C1, -C2, -C3, -C4 and protalus rampart MK-B2. The photo was taken on June 30th 2012. As in Fig. 5, yellow and light blue dashed lines correspond to landforms of morainic complexes MK-B and MK-C, respectively.

All three calculated ages of 12.40 ± 0.90 ka (MK-11), 15.5 ± 1.1 ka (MK-12) and 8.6x ± 0.6x ka (MK-13) fail to meet the χ^2 criterion test. Sample MK-13 provided the youngest age (8.6x ± 0.6x ka) and was rejected as an outlier, because the mean ages of the moraines that are located further inboard were older, as presented below (Fig. 9C). This boulder was most likely affected by post-depositional movement, as can also be suspected from its instable position. Concerning the other two samples from moraine MK-B1, boulder MK-12 (15.5 ± 1.1 ka) is embedded in a stratigraphically lower position than MK-11 (12.40 ± 0.90 ka), consistent with their progressively younger ^{36}Cl ages (Fig. 4, Tables 2 and 3). Therefore, we attribute their age offset primarily to different phases of moraine formation resulting from recurrent glacier advances of equal extent. We consider the oldest age (sample MK-12: 15.5 ± 1.1 ka) as the most relevant for the timing of moraine MK-B1 deposition, which along with the age of sample TZ-03 (15.6 ±1.1 ka), mark the beginning of an early Late-glacial moraine stabilization phase on Mount Olympus.

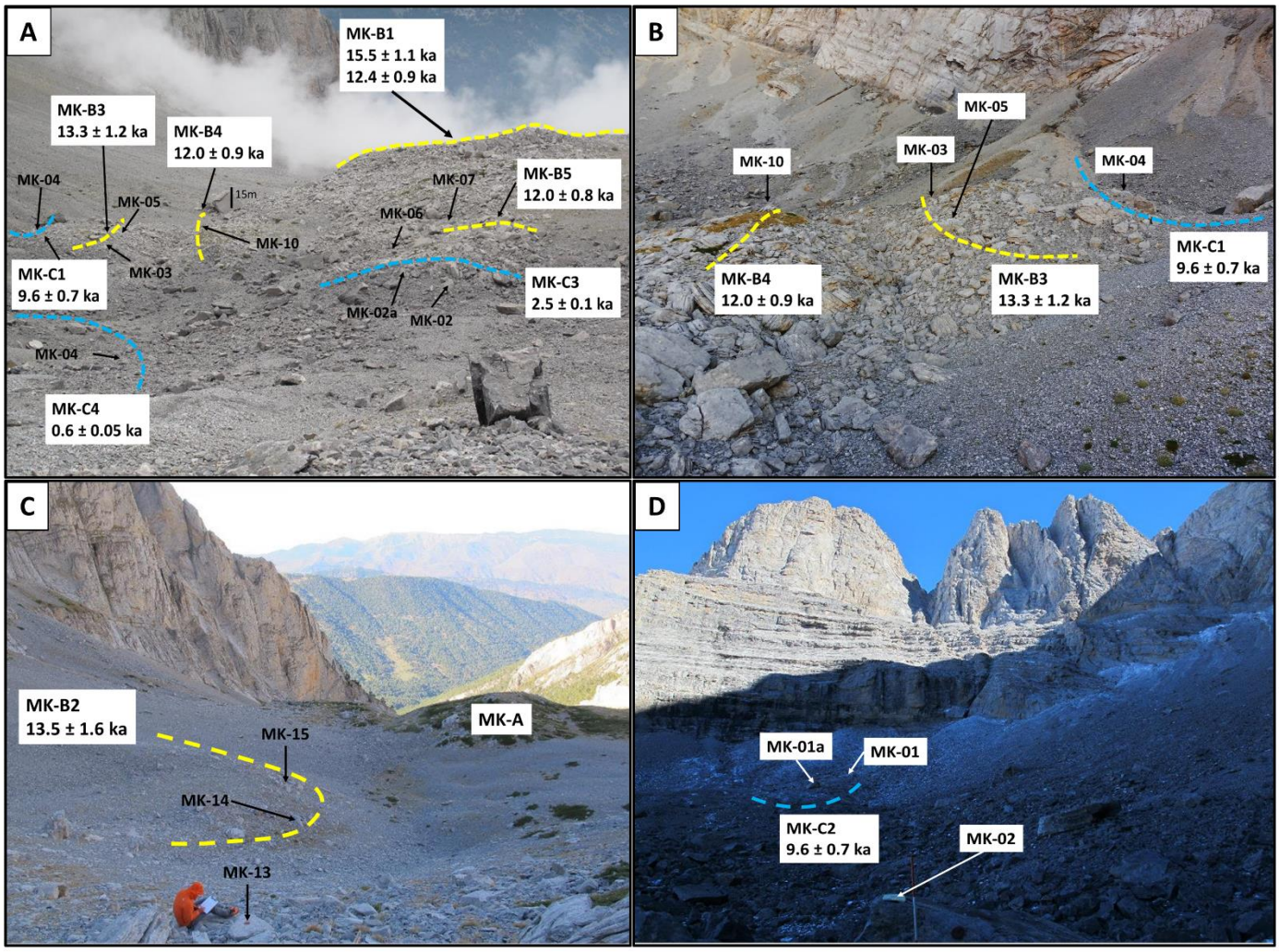

Fig. 9. Field photos of sampled boulders and landforms in MK cirque. A) General view in the down-valley direction of frontal moraines MK-B1 and MK-B3, hummocky moraines MK-B4 and MK-B5, together with the late Holocene moraines MK-C3 and MK-C4, with the locations of individual samples. B) Closer view in the upvalley direction of moraine MK-B3, together with nested moraine MK-C1 and hummocky moraine MK-B4. C) Moraines MK-A and MK-B2 located stratigraphically below frontal moraine MK-B1 (outlier sample MK-13 is also indicated). The photo was taken from the crest of moraine MK-B1 with view in the down-valley direction D) Early Holocene moraine MK-C2, situated close to the cirque headwall at the apex of the outwash plain. The photo was taken from the crest of the late Holocene moraine MK-C3. View in upvalley direction.

Along its western end (west of the cirque centre line, Fig. 5), moraine MK-B1 is dissected by push moraine MK-B2 (Figs 5, 8 and 9C). Two boulder samples, embedded in the outer slope of MK-B2, yield ages of 14.6 ± 1.0 ka (MK-14) and 12.43 ± 0.86 ka (MK-15), with a mean age of 13.5 ± 1.5 ka (Fig. 7B).

Further inboard of MK-B1 and closer to the cirque cliffs (southwest of the cirque centerline and below the high walls of Skolio), two boulders were sampled along the outer crest of moraine MK-B3 (Figs. 5 and 9B), yielding ages of 12.47 ± 0.91 ka (MK-03) and 14.2 ± 1.0 ka (MK-05) with a mean age of 13.3 ± 1.2 ka (Fig. 7). The formation of moraines MK-B2 and MK-B3, is related to excess of wind-blown snow accumulation deposited during a period with enhanced aeolian activity from the cliffs above.

Also inboard of frontal moraine MK-B1 but closer to the cirque center, the apron of large-sized (> 0.5m) blocks with high degree of fragmentation (Fig. 5, 8 and 9A) is interpreted as englacial or supraglacial debris, deposited as the MK paleoglacier was retreating. This may have occurred either soon after the early Late-glacial phase of Mount Olympus moraine stabilization (~15.5 ka ago), or later after a second phase of Late-glacial glacier activity (~12.5 ka), which was probably associated to very cold conditions causing the fragmentation of these boulders. Boulder MK-10 on MK-B4 yielded an age of 11.97 ± 0.9 ka, and boulder MK-07 on MK-B5 gave an identical age of 12.06 ± 0.78 ka. We consider the ages of these hummocky moraines as representing the end of the second Late-glacial phase of glacial activity on Mount Olympus.

The subsequent stages of glacier dynamics in MK cirque correspond to the deposition of moraine group MK-C and are of Holocene age. Blocky moraine MK-C1, which is nested within moraine MK-B3 close to the southwestern part of the cliff (Figs 5, 8, 9A and 9B), was dated to 9.64 ± 0.71 ka based on boulder sample MK-04. Two boulder samples were collected from another blocky moraine, MK-C2, which is

located in an approximately symmetrical position compared to MK-C1 relative to the cirque center line (Fig. 5), and yielded ages of 9.62 ± 0.71 ka (MK-01) and 16.8 ± 1.2 ka (MK-01a) (Table 3). The old age of sample MK-01a is incompatible with the rest of the moraine chronology in MK glacial cirque, most likely due to inherited ^{36}Cl concentrations from previous exposure periods, and it was thus considered an outlier and discarded from the discussion. The age of boulder MK-01 is identical with that of boulder MK-04 from moraine MK-C1, implying that both moraines MK-C1 and -C2 were formed at the same time (~9.6 ka ago) as a result of a common forcing mechanism that restricted the ice extension along the perimeter of the cirque close to the bounding cliffs. Their deposition is therefore attributed to an early Holocene glacier re-advance or standstill, as the MK paleoglacier was retreating from its larger late Late-glacial extent. From our chronology we cannot draw further conclusions whether following this early Holocene glacier extent, MK paleoglacier persisted in sheltered locations close to the cirque headwalls, or disappeared entirely during the mid-Holocene. The next phase of glacial activity on Mount Olympus is evident from the central frontal moraine MK-C3 (Fig. 5, 8, 9A), dated with three boulders samples to 2.59 ± 0.17 ka (MK-02), 2.58 ± 0.19 ka (MK-02a), 2.36 ± 0.19 ka (MK-06), with a mean age of 2.51 ± 0.13 ka (Fig. 7). The corresponding late Holocene glacier likely occupied a similar or slightly larger area in relation to the early Holocene standstill boundaries (Figs 10F, G). Finally, blocky moraine MK-C4 is confined close to the southern cirque margins, 100m below the terminus of the present-day permanent snowfields lower boundary (Styllas, 2016). The single date of 0.64 ± 0.05 ka (boulder MK-09) from this moraine places its formation within the early part of the Little Ice Age. It is also likely that the formation of MK-C4 in such protected location can be attributed to a large degree to the local topoclimatic factors, the most important being the accumulation of wind-blown and avalanching snow during the winter and shading from the cliffs above during the summer (Fig. 5, 8, 9A).

Noteworthy is the absence of landforms of similar age in the Throne of Zeus cirque, which highlights the importance of orientation among other topoclimatic factors (height of headwalls, wind-blown snow, shading etc.) for the formation and evolution of Mediterranean cirque glaciers.

5. The tempo of Mount Olympus glacial history in relation to regional glacial, lacustrine and marine environments

Based on our calculated landform ages and geomorphological investigations in the Throne of Zeus (TZ) and Megala Kazania (MK) cirques, we propose a chronological sequence of Mount Olympus glacial history, and compare it with the existing SED studies from the northeast Mediterranean mountains and with paleoclimate proxies from regional terrestrial and marine environments. In this section, we show the individual ^{36}Cl ages and arithmetic mean ages with their full uncertainties (including production rates, see section 3.2), to allow for comparison with chronologies based on other dating methods (Table 3, Fig. 7). We note that the error ranges of the landform ages permit us to only tentatively relate our findings to specific paleoclimate periods, such as the Oldest Dryas (17.5 – 14.7 ka, Rasmussen et al., 2006) and the Younger Dryas (12.7 – 11.5 ka - Alley, 2000), which are temporally well-constrained from regional continuous high resolution paleoclimatic records, e.g. from the records of oxygen isotope changes in Greenland ice cores. We rather assign the distinct phases of glacial activity on Mount Olympus to the early, middle and late stages of the Late-glacial and to the early (11.7 – 8.2 ka) and late (4.2 – 0 ka) Holocene (Walker et al., 2012). However, it must also be noted that the chronological order of our ^{36}Cl mean ages in both glacial cirques is in very good agreement with the landform stratigraphy, thus strongly supporting the general temporal sequence of glacier fluctuations that we infer from our ^{36}Cl chronology.

5.1 The Late-glacial and Holocene glacial chronology of the northeast Mediterranean Mountains

The first phase of glacial activity within the TZ and MK cirques with respective ELAs at ~2600m and ~2200m, is derived from the individual ages of samples TZ-03 (15.6 ± 2.0 ka) and MK-12 (15.5 ± 2.0 ka), which are considered to represent the minimum ages of stabilization of frontal moraines TZ-A and MK-B1, respectively (Fig. 10A, B). By taking into account the small surface area and the altitudinal extent of the cirques under consideration, we assume no significant differences between the local ELA and the glacier termini. In the following discussion, we refer to this time as the "early Late-glacial stage 1" (LG1). The LG1 timing of moraine stabilization is in good agreement with ^{10}Be ages of glacial landforms from Šara Range and Mount Pelister (SW Balkan mountains) and from Mount Uludağ's east Karagol valley and West Ski Area in NW Turkey (see Fig. 1 for locations), where glacier advances with termini between 2000m and

2200m occurred no later than 16.4 ± 1.3 ka, 15.2 ± 0.85 ka, 15.9 ± 1.1 ka and 15.2 ± 1.0 ka respectively (Fig. 11) (Kuhlemann et al., 2009, Ribolini et al., 2017, Akçar et al., 2014, Zahno et al., 2010). Note that for comparison, the single-boulder age from Šara Range (16.4 ± 1.3 ka, Kuhlemann et al., 2009) was recalculated using the same calculator and parameters as in Ribolini et al. (2017) and Akçar et al. (2014), i.e. the online CRONUS-Earth calculator version 2.2 with the NE North American production rate and the time-dependent "Lm" scaling scheme (Balco et al. 2008, 2009). The concentration of this sample measured at the ETH tandem facility in Zürich relative to laboratory standard S555 (Kubik and Christl, 2010) was multiplied by 0.9124 to normalize to the 07KNSTD standard (Akçar et al., 2011). The ^{10}Be ages by Zahno et al. (2010) had already been recalculated accordingly, by Akçar et al. (2014).

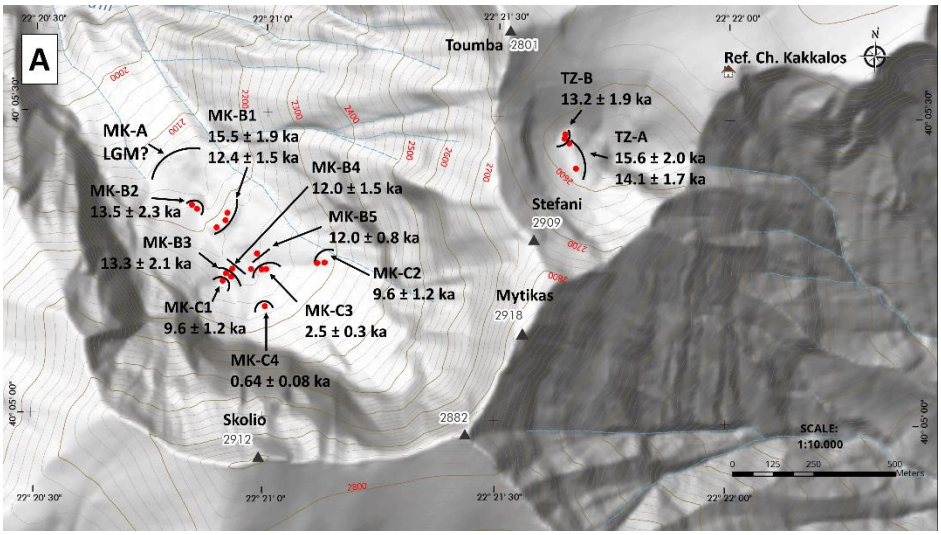

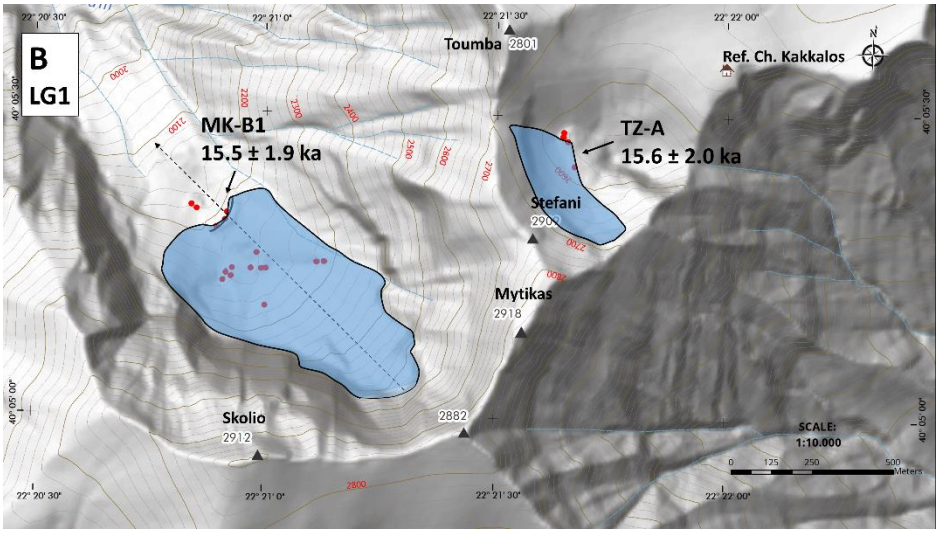

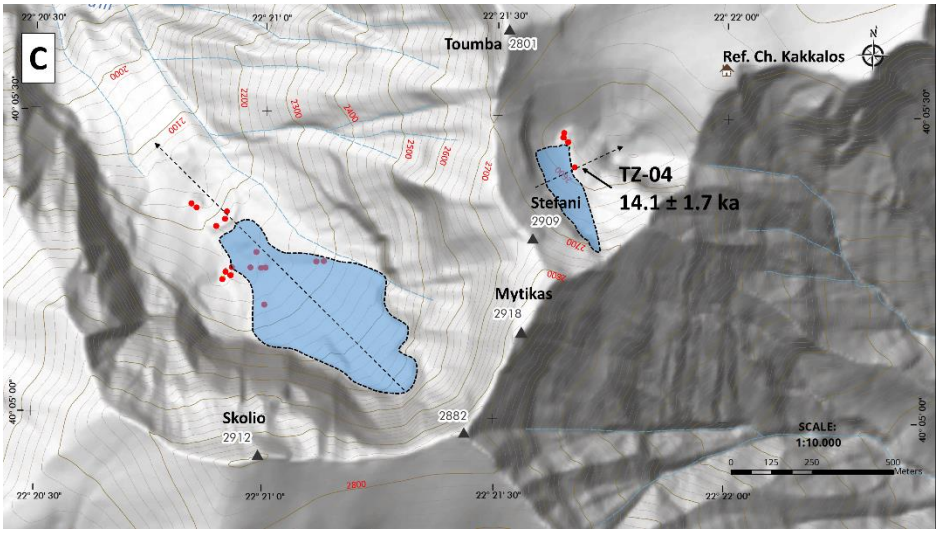

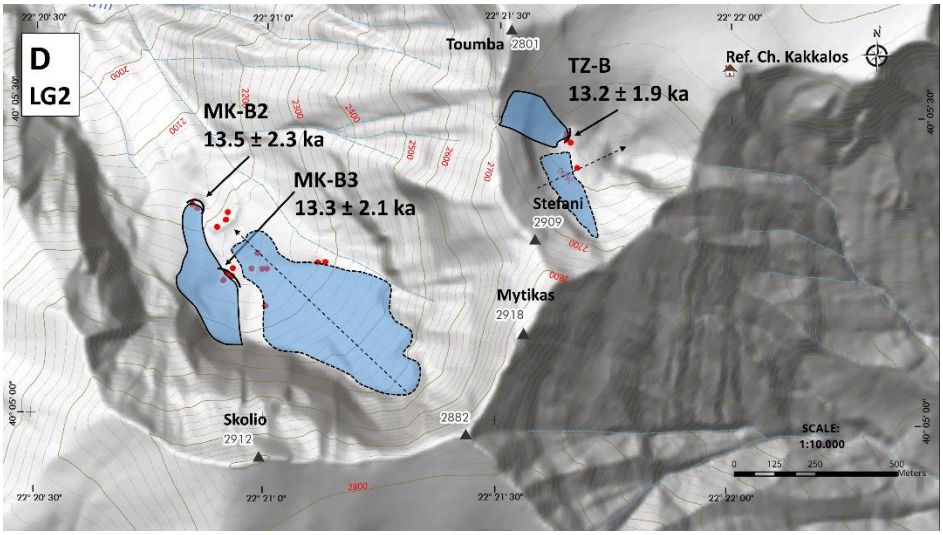

549
550

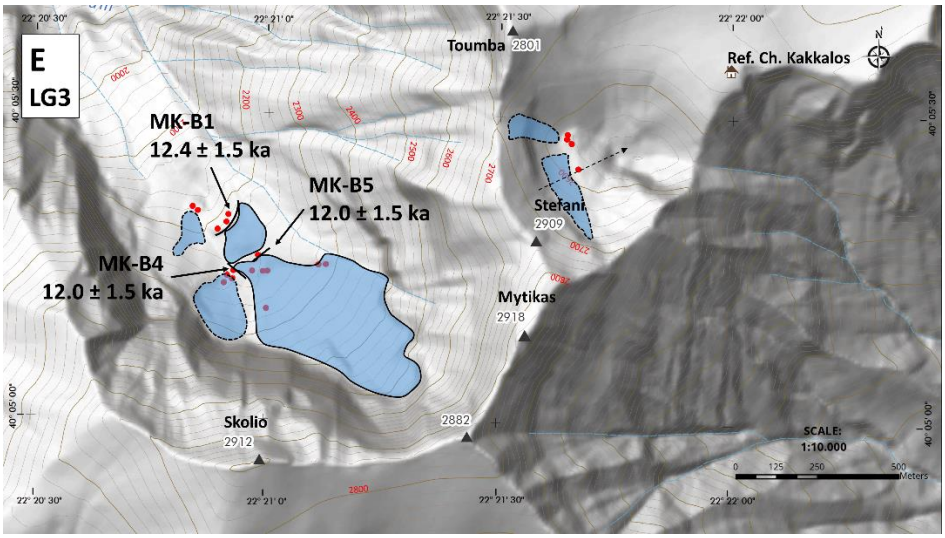

551
552

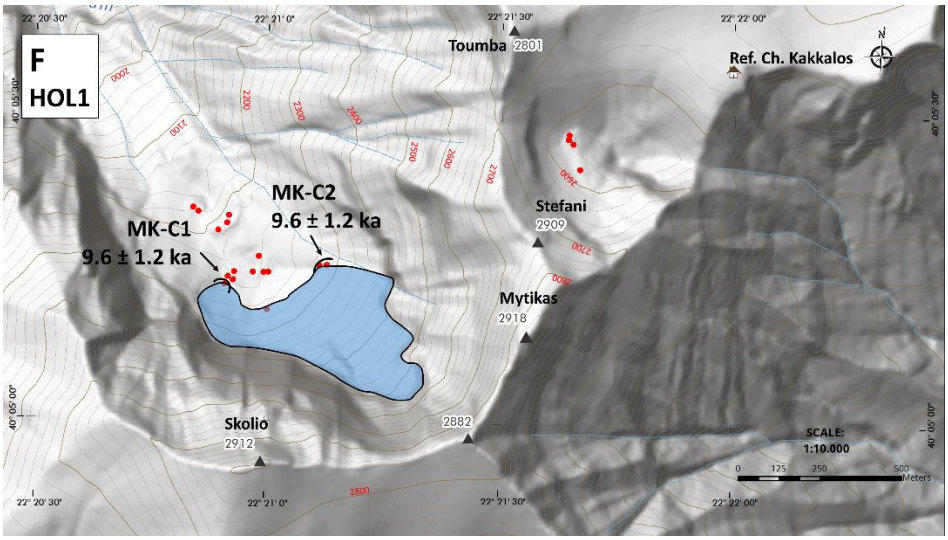

553
554

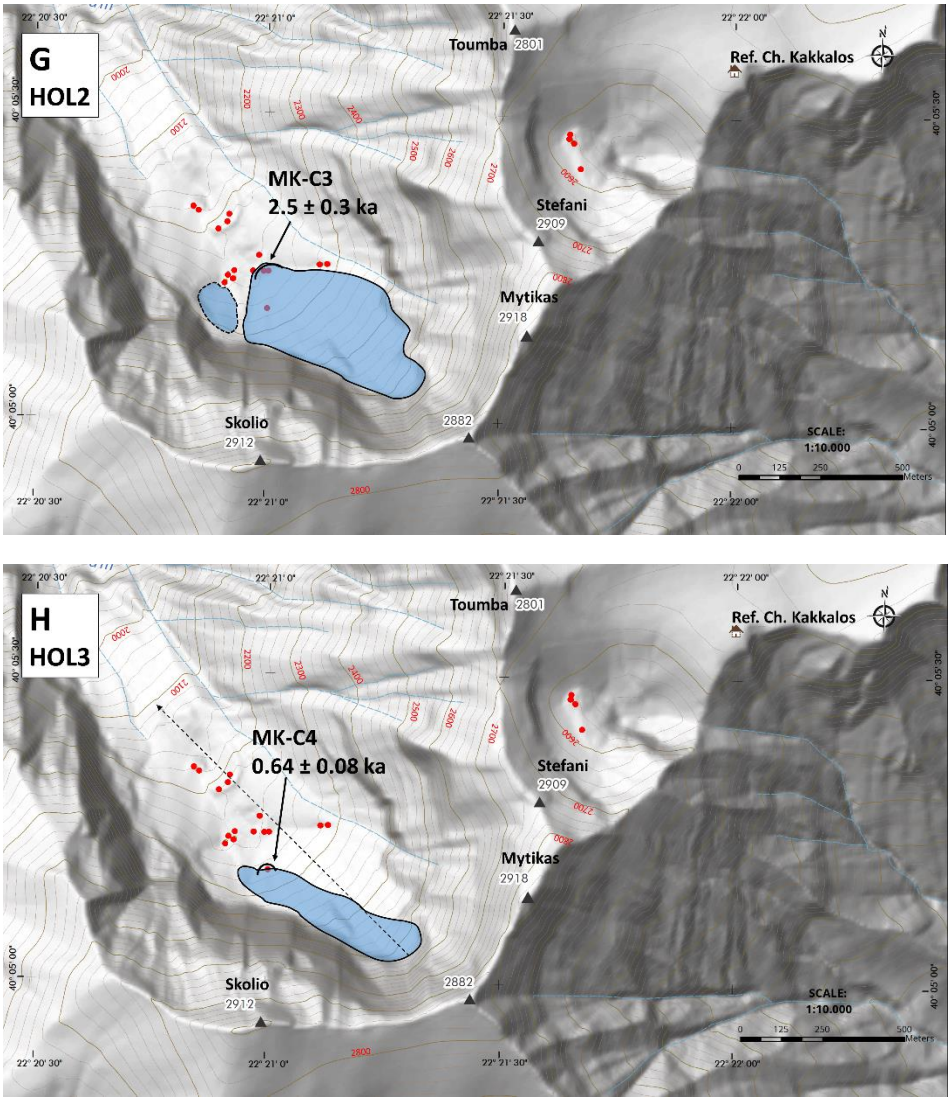

Fig. 10. Reconstrunctions of the Late-glacial and Holocene evolution stages of TZ and MK paleoglaciers, with the respective moraines and/or individual samples that delimit the glacier extensions of each stage. A) Dated landforms with mean ages (arithmetic mean) and individual samples ages, where only one sample was used to date the landform, or where the χ^2 criterion test failed. All ages include the full range (analytical and production rate) errors. Red dots correspond to the individual samples and black curved lines to the individual moraines shown in Fig. 2. In panels B to H, blue areas delimited by dashed lines correspond to approximate spatial boundaries of the paleoglaciers, tentatively defined by the analyses of this study. B) Early Late-glacial (15.5 ± 2.0 ka) stabilization phase (LG1) of moraines TZ-A and MK-B1. C) Early Late-glacial (14.1 ± 1.7 ka) retreat phase. D) Mid Late-glacial stabilization phase (LG2) of moraines TZ-B and MK-B3 and push moraine MK-B2, under windier conditions (13.5 ± 2.0 ka). E) Late Late-glacial (LG3) glacier shrinking under cold conditions with deposition of hummocky moraines MK-B4 and -B5, related to the Younger Dryas. F) Early Holocene glacier standstill phase (HOL1) with exposure of moraines MK-C1 and – C2 at 9.6 ± 1.2 ka. G) Late Holocene stabilization phase (HOL2) of moraine MK-C3 (2.5 ± 0.3 ka). H) Little Ice Age glacier expansion (HOL3) at 0.64 ± 0.08 ka.

On Mount Olympus, the temporal and spatial extents of TZ and MK paleoglaciers shortly after the LG1 moraine stabilization phase, cannot be defined with certainty from the existing data. The LG1 glacier extension phase was most likely followed by a gradual deglaciation, as manifested by the exposure age of 14.1 ± 1.7 ka of bedrock sample TZ-04. (Fig. 10C).

Recently, Gromig et al., (2017) used ^{36}Cl to date the stabilization of five limestone boulders on a moraine in the Galicica Mountains in SW Balkan Peninsular (Fig. 1), and related its formation to the Younger Dryas based on the mean moraine age of 12.0 ± 0.6 ka. The mean moraine age was corrected for an erosion rate of 5 mm/ka and for a snow cover factor of 0.98. The age calculations were done using a ^{36}Cl production rate for spallation of Ca (Marrero et al., 2016) higher by ~20% than the one we use in our study, and the uncertainty in mean age does not include the production rate errors. For the sake of comparison, we recalculated the five boulder ages using the same ^{36}Cl production and scaling parameters as applied for our samples, and taking into account the erosion and snow corrections locally suggested in Gromig et al. (2017) (5 mm/ka erosion; snow cover factor of 0.98). This resulted in a mean moraine age and full error of 14.0 ±

1.8 ka. We suggest that this latter age is in better agreement with other evidence of glacial behavior in this region based on the following observations. The dated moraine in the Galicica Mountains is located at an elevation of 2030m and is the largest and second-to-outmost one in a series of several moraines. On Mount Pelister, located 30km to the east across Lake Prespa (Fig. 1), the most prominent of a series of moraines located at an elevation of 2230m, composed of quartz-bearing lithologies, was dated with ^{10}Be (for which the production rate is well constrained) to a mean age of 15.2 ± 0.85. The formation of this moraine was assigned to the Oldest Dryas glacial advance (Ribolini et al., 2017). Given, 1) the proximity between the two sites in the Galicica Mountains and on Mount Pelister, 2) the similar north-eastern orientation of both glacial cirques and 3) the ~200 m higher elevation of the Oldest Dryas moraine on Mount Pelister, we suggest that a Younger Dryas age for the moraine in the Galicica Mountains is rather unlikely. We further propose that the moraine sequences in both the Galicica Mountains (Gromig et al., 2017) and on Mount Pelister, like in the case of Megala Kazania, can be related to a series of Late-glacial successive advances of similar extent.

The LG1 glacial phase is different from a preceding glacial phase recorded in Rila Mountains (~18–16 ka), and which has been ascribed to a late stage of the LGM (Kuhlemann et al., 2013). On Mount Olympus, this pre-LG1 glacial phase is likely represented by the stabilization of moraine MK-A (Fig. 9C and 10A). We thus conclude that moraine stabilization during LG1 glacial phase in the northeast Mediterranean mountains occurred at ~15.5 ka with an ELA at ~2200m in the north/northeast facing cirques of Šara Range, Galicica Mountains, Mount Pelister, Mount Uludağ and MK, and at ~2600m in the east facing TZ cirque and terminated as the glaciers began to retreat at ~14.0 ka (Fig. 11). Within uncertainties, the LG1 glacial phase can be tentatively ascribed to a late stage of the Oldest Dryas (Fig. 11), which ended ~14.7 ka ago (Rasmussen et al., 2006). This is in line with the postulation by Hughes et al (2003, 2006a) that optimal conditions for Mediterranean glaciations occurred in intermediate periods between major stadials and interstadials, as during major stadials reduced moisture availability was not sufficient to promote glaciation.

The glacier retreat phase at ~14.0 ka (Fig. 10C) was followed by a return to glacial conditions with the stabilization of moraines MK-B2 (13.5 ± 1.6 ka.), MK-B3 (13.3 ± 1.2 ka) and TZ-B (13.2 ± 1.9 ka), suggesting a common forcing mechanism (Fig 10D). The stabilization of the three moraines occurred during a mid-Late-Glacial period of climatic change, which we define here as the Late-glacial stage 2 (LG2), (Fig. 11). The stabilization of moraines TZ-B, below the saddle separating the summits of Stefani (2909m) and Toumba (2801m), and of MK-B2 and -B3 below the 500m north facing headwall of Skolio (2912m) (Fig. 2), can be attributed to excess accumulation of wind-blown and avalanching snow related to wind activity from a general western direction (Figs. 3, 10D). The increased deposition of wind-blown snow likely occurred in marginal conditions for glaciation, as suggested by the regional warmer conditions around ~13-14 ka that are recorded in numerous lacustrine and marine sedimentary records along the northeast Mediterranean (see section 5.2). The warmer and windier conditions during LG2, terminated with another return to glacier friendly conditions during the late Late-glacial, as suggested by sample MK-11 (12.4 ± 1.5 ka), which might denote a post-depositional reactivation of frontal moraine MK-B1. The third phase of glacial activity during the Late-glacial stage 3 (LG3), is associated with the stabilization of hummocky moraines MK-B4 and -B5 (Figs 10E, 11). Their positions, 150m inboard and 20m higher relative to frontal moraine MK-B1 and closer to the center of the cirque, suggest that LG3 was characterized by glacier decay. Observations from the Svalbard region and studies of Younger Dryas moraines in Scotland relate the formation of hummocky moraines to changes in the glacier thermal regime from temperate to polythermal, with warm-based ice in the interior and cold-based ice in the glaciers margins (Hambrey et al., 1997). Therefore, it is likely that the formation and exposure of the hummocky moraines MK-B4 and MK-B5 at 12.0 ± 1.5 ka corresponds to a significant drop in air temperatures, also evident from the cryogenic features within the sedimentary sequence of Theopetra cave (Fig. 1, Karkanas, 2001). This implies that conditions were cold enough and moisture availability was considerably low during LG3, resulting in an overall cold and dry phase of glacier decay, which is most likely responsible for the intense fragmentation of the boulder apron inboard of moraine MK-B1. Within dating uncertainties, we ascribe the LG3 glacial phase, characterized by glacial decay to the Younger Dryas (Alley et al., 1997).

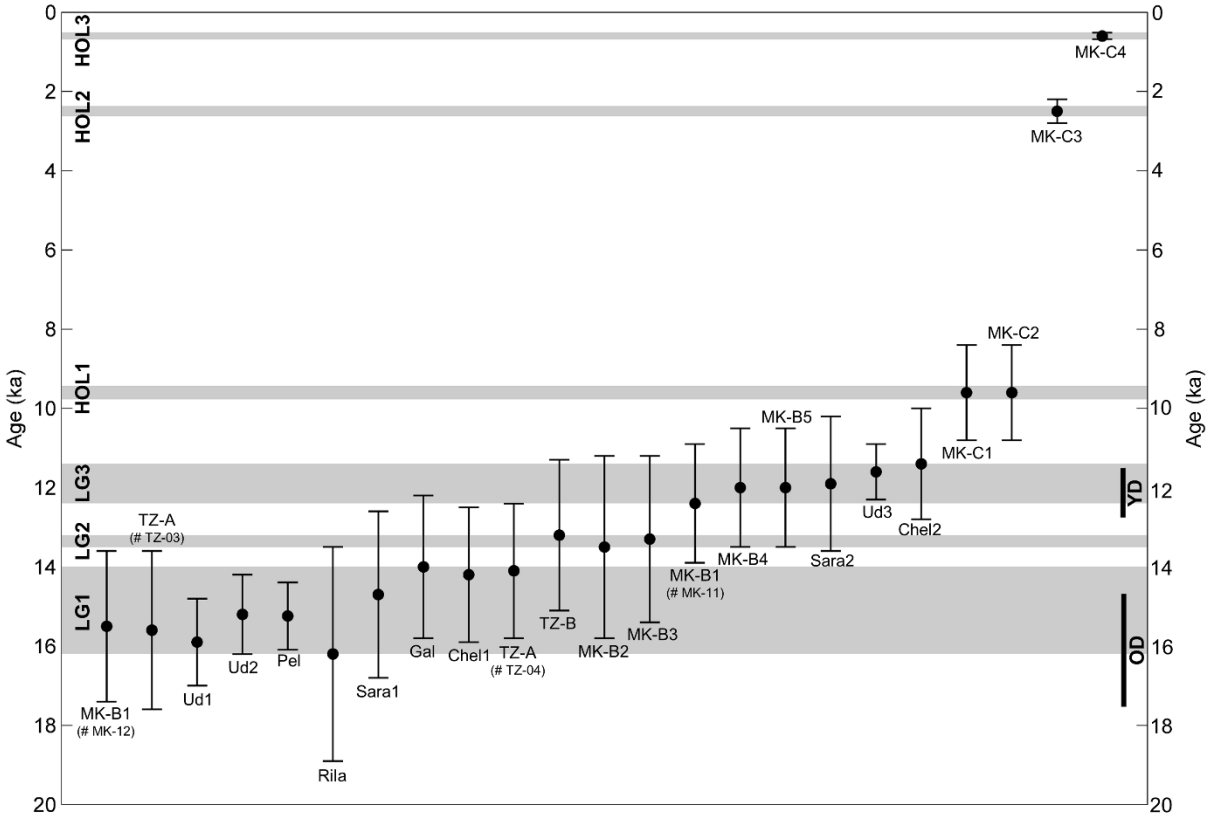

Fig. 11. The Late-glacial and Holocene glacial chronology of the northeast Mediterranean mountains based on SED of glacial landforms. Glacial phases (LG1-3, HOL1-3), resulted from the minimum and maximum mean ages of the dated landforms. Mount Olympus landforms MK-B1 and TZ-A are represented by two separate samples each (shown in parentheses), while the others are represented either by a single sample, or by the arithmetic mean of the independent ages that meet the χ^2 criterion (Fig. 7). Other landforms include SED from: Ud1: Uludağ Mountain Karagöl Valley (Akçar et al., 2014). Ud2: Uludağ Mountain West-Ski Area (Zahno et al., 2010). Pel: Mount Pelister (Ribolini et al., 2017). Rila: Rila Mountains (Kuhlemann et al., 2012). Sara1: Šara Range sample S16 (Kuhlemann et al., 2009). Gal: Galicica Mountains (Gromig et al., 2017), arithmetic mean of the recalculated ages with the same parameters of this study. Chel1, 2: Mount Chelmos samples from Kato Kambos valley (Pope et al., 2015), recalculated with the same parameters of this study. Sara2: Šara Range sample S7 (Kuhlemann et al., 2009). Ud3: Uludağ Mountain West-Ski Area (Zahno et al., 2010). The temporal boundaries of the Older Dryas (Rasmussen et al., 2006) and the Younger Dryas (Alley et al., 1997) periods, are shown.

Despite the ~350 m elevation difference between the frontal moraines MK-B1 in MK cirque (2225m) and TZ-A in TZ cirque (2580m), both moraines formed during the same period (LG1). This can be explained by the different topographical configurations of the two cirques. MK cirque has a NW orientation, is bounded by 500m high headwalls, receives higher amounts of windblown snow and has a longer period of shading. These geomorphological characteristics permit the formation of a larger and more protected glacier that extended to lower altitudes and occupied a surface area 3 times larger (1 km long, 0.5 km wide) compared to the TZ paleoglacier. Due to these topographic attributes, deglaciation of the MK paleoglacier was much slower than that of TZ paleoglacier. This becomes particular apparent from the fact that the glacier survived after the LG1-3 phases evident from the deposition of morainic complex MK-C, which corresponds to glacier extents during the early (11.7 – 8.2ka) and late (4.2 – 0ka) Holocene (Walker et al., 2012). Geomorphological evidence of Holocene glaciation are also present as glacier activity in Šara Range (Kuhlemann et al., 2009) and the Rila Mountains (Kuhlemann et al., 2013), but are either obscured and/or absent from Galicica Mountains, Mount Pelister and TZ cirque. We interpret the early Holocene blocky moraines MK-C1 and -C2 at 9.6 ± 1.2 ka, located close to the cirque headwalls, as representative of a glacier standstill or short readvances (HOL1, Fig. 11), during a general early Holocene phase of warming and glacier retreat (Fig. 10F). The late Holocene glacier expansions (Fig. 10G and H) with stabilization of moraines MK-C3 and MK-C4 at 2.5 ± 0.3 ka and 0.6 ± 0.08 ka (Fig. 11), respectively, may be explained by a return to wet winters and cool summers that promoted the last glaciation phases on Mount Olympus.

5.2 Correlations of Mount Olympus glacial chronology with regional terrestrial and marine records

In this section, we correlate our new glacial chronologies with selected paleoclimatic proxies, in order to investigate possible external and internal climatic forcing mechanisms responsible for the climate changes that are recorded by the glacial landforms on Mount Olympus. We emphasize again that these correlations must be considered tentative given the uncertainties in the cosmogenic nuclide ages.

Phase LG1 characterized by moraine stabilization within the TZ and MK cirques and subsequent glacier recession at ~14.0 ka (Fig. 11), coincides with a cycle of peak solar insolation, as expressed by the Optical Depth of Luminescence (ODL) in Duhlata Cave (Fig. 12A). Despite the fact that the theoretical solar insolation curves by Berger and Loutre (1991) are the most accredited in paleoclimate reconstructions, they explain about ½ of the paleoclimatic signal (e.g. Imbrie et al., 1993). For this reason we use here the ODL record from the proximal (280km to the northeast, Fig. 1) to Mount Olympus Duhlata Cave. The ODL is derived from the calcite speleothem luminescence of organic material, which also takes into account the solar luminosity and thus considered an indirect regional proxy of solar radiation (Stoykova et al., 2008). Superimposed on this peak solar insolation cycle, is the change of the regional climate from cold and dry to warmer and wetter, suggesting an *out-of-phase* behaviour. The cold and dry climate during LG1 is registered in the lacustrine records of Lakes Prespa, Ohrid and Tenaghi Philippon (Fig. 12C, D, E). The two former lakes are located 140km west of Mount Olympus at elevations of 690 and 850m, with their watersheds bounded by Galicica Mountains and Mount Pelister, whereas the latter is located 190km to the northeast of Mount Olympus at an elevation of 50m. The existence of steppic taxa such as *Artemisia* and *Chenopodiaceae*, in Lake Prespa (Aufgebauer et al., 2012) and in Tenaghi Phillipon (Fig. 12E) (Pross et al., 2015, Wulf et al., 2018), indicate regional dry conditions. This is further supported by the low $CaCO_3$ values in Lake Ohrid, which suggest low allochthonous carbonate sediment input from the catchment (Fig. 12D), likely due to reduced surface runoff (Vogel et al., 2010). Quantitive pollen-based temperature and precipitation reconstrunctions from Lake Maliq (located 20km south of Lake Ohrid and 10km west of Lake Prespa, Fig. 1), suggest that between 16–15 ka, the mean annual temperature ranged from -3 to 1^{o}C and the mean annual precipitation was 400mm, whereas present values are 11.2^{o}C and 790mm, respectively (Bordon et al, 2009). At lower elevations along the Aegean Sea, this period was characterized by relatively cool (14.5^{o}C) Sea Surface Temperatures (SST) (Fig. 12F), by an expanse of *Pinus* (Fig. 12G) (Kothoff et al., 2011), by increased fluvial sediment inputs (Fig. 12I) and by coarser grain-sized sediments (increased silt fractions) on the bottom of the north Aegean Sea (Fig. 12J). This can be explained by the fact that vegetation was sparse along the upper parts of watersheds and glacial conditions produced coarser sediments containing higher amounts of silt. Despite the overall cold conditions in the higher (>800m) elevations, precipitation starvation combined with high solar insolation (Fig. 12A), are considered as the likely causes that restricted the expansion of glaciers within the cirques at elevations between 2000 and 2200m. The transition to warmer and wetter climatic conditions towards the later part of LG1, resulted in the gradual deglaciation of the northeast Mediterranean cirques, which together with increasing annual precipitation (Bordon et al. 2009) and SST's (Fig. 12F), contributed to an expansion of *Quercus* forests and to increasing fluvial inputs, with higher amounts of fine fractions in the Aegean Sea (Fig. 12J).

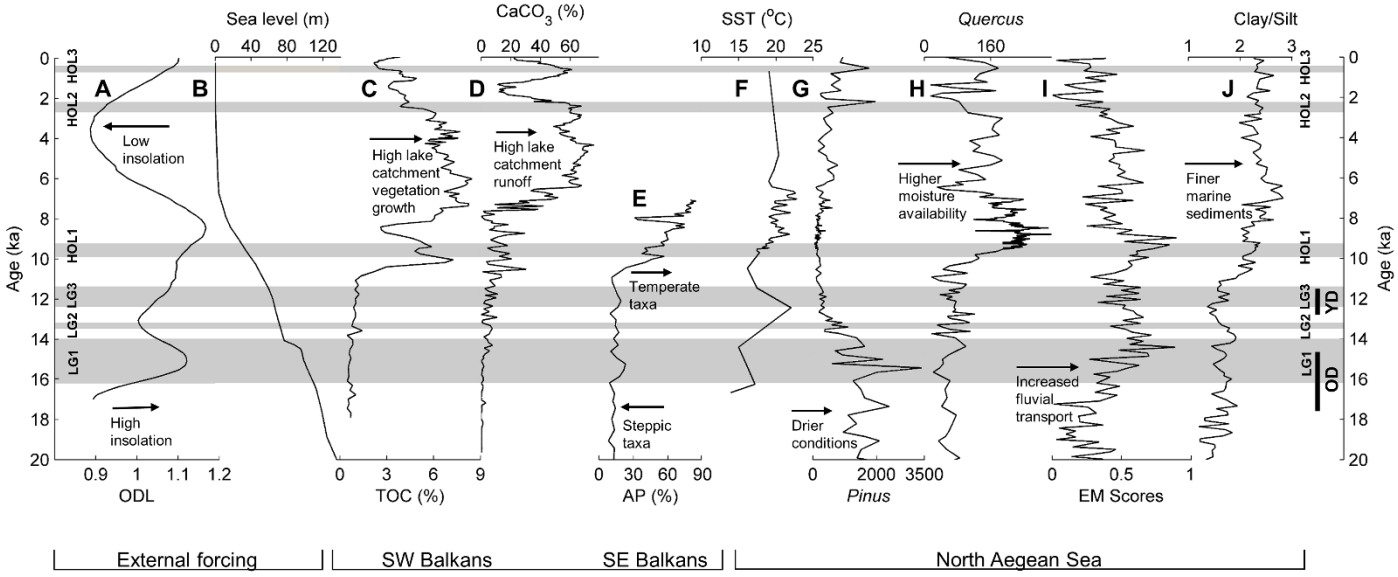

Fig. 12. Correlation of the Late-glacial and Holocene glacial phases (LG1-3 and HOL1-3) derived from the compilation of SED-based glacier chronologies from the northeast Mediterranean mountains (Fig. 11), with selected external forcing, terrestrial and marine proxies. A) Optical Depth of Luminescence, Duhlata Cave (Stoykova et al., 2008). B) Ice-volume equivalent sea-level function, expressed as m below present sea level (Lambeck et al., 2014). C) Total Organic Carbon from Prespa Lake (Aufgebauer et al., 2012). D) $CaCO_3$ concentrations from Lake Ohrid (Vogel et al., 2010). E) Tenaghi Philippon Arboreal Pollen (AP) concentrations (Wulf et al., 2018). F) North Aegean Sea SST's (°C) (Core MNB-3, Gogou et al., 2007). G) *Pinus* and H) *Quercus* pollen counts from marine core SL-152 (Kothoff et al., 2008). I) End-member 2 (EM2) scores representative of fluvial input from marine core SL-148 (Hamman et al., 2008). J) Clay/Silt fraction of marine core SL-148 as a proxy of grain-size and glacial versus interglacial conditions (Ehrmann et al., 2007).

On Mount Olympus, the deglaciation that concluded LG1 was followed by glacial phase LG2 (Fig. 11), despite the rapid changes of the regional climate. Bordon et al. (2009) suggest the occurrence of an abrupt warming on the order of 10°C after LG1 (~15 ka), deduced from a sediment core record in Lake Maliq (elevation 690m) with mean annual temperatures 7-10°C. In north Aegean Sea a sharp increase in lipid biomarker-derived SST from 14.5°C to 22°C is recorded in core MNB 3 (Gogou et al, 2007, Fig. 1) between 14.5 and 12.5 ka (Fig. 12F). However, the stabilization of moraines MK-B2, -B3 and TZ-B during LG2, implies that despite the regional warming, the conditions on Mount Olympus remained favourable to glaciation, and we attribute this mainly to excess wind-blown snow accumulation and to solar insolation minima (Fig. 12A). The enhanced aeolian activity on Mount Olympus is also represented in Lakes Ohrid and Prespa sediment records by the increased amounts of sand in the bottom sediments, which have been related to subaqueous current activity under an intense wind stress field (Vogel et al., 2010). During the same time interval, the sea-level had risen from its LGM lowstand (-120 m) to a depth of -70m (Fig 12F), and was distanced 35km from TZ and MK cirques. It is therefore plausible that the shallow waters and high SST's may have resulted in increased evaporation and cloudiness especially during the warmer summer season, which combined with solar insolation minima and with high amounts of wind-blown snow during the winter, resulted in marginal glacier-friendly conditions on Mount Olympus during LG2.

Phase LG3 of glacier shrinking under cold and dry climate on Mount Olympus, finds firm evidence in Šara Range, Rila Mountains and Mount Uludağ (Figs 1 and 11). Similarly to LG1, glacial phase LG3 is characterized by a decoupling between solar insolation, which was increasing, and temperature and precipitation, which were low; these conditions were rather favourable to glacier shrinking (Fig. 12A). The cold and dry conditions during LG3 are related to the Younger Dryas, which affected the terrestrial and marine systems of the broader region to an equal or even to a greater extent than LG1. Terrestrial cooling in the SW Balkans (Lake Maliq) was 11°C and P_{ann} was reduced by 50% to 300-400mm (Bordon et al., 2009). The climatic conditions during LG3 resulted to minor forest contraction in the intramontane basin of Ioannina Lake (Lawson et al., 2004), located 35km south of Mount Tymphi and 135km west of Mount Olympus (Fig. 1), but did not favor the formation of glaciers in Mount Tymphi (Pope et al., 2015). This implies that during LG3 moisture availability in the SW Balkans was marginal to sustain forest vegetation

but not to promote glaciation in Mount Typmhi, the opposite holding truth for Mount Chelmos in southern Greece (Fig. 1), where two samples with ^{36}Cl ages of 11.4 ± 1.4 ka and 14.2 ± 1.7 ka, were recalculated using the same parameters as in this study (Pope et al., 2015, Fig. 11). The Younger Dryas glaciation in Mount Chelmos has been attributed to a southern deflection of the Mediterranean storm tracks (Pope et al., 2015), in a similar manner that ocurred during the LGM (Kuhlemann et al., 2008). A different paleoclimatic pattern in the SE Balkans arises from ELA reconstrunctions based on geomorphological evidence and stratigraphic correlations from the Rila Mountains (Kuhlemann et al., 2013), and from SED's from Šara Range (Kuhlemann et al., 2009), from Mount Uludağ West Ski area (Zahno et al., 2010) and from TZ and MK cirques on Mount Olympus (Fig. 11). Glacier shrinking on Mount Olympus during LG3, was coupled by a less pronounced drop in SST's, which was in the order of 6^{o}C (Gogou et al., 2007, Kothoff et al., 2011). A similar situation occurred in the north Aegean Sea, during the "8.2ka event", and was characterized by considerably colder conditions, when continental cooling in Tenaghi Philippon and the Rhodope Mountains (Fig. 1) was much more intense (Pross et al., 2009), in comparison to the north Aegean borderlands (Kothoff et al., 2008, 2011). LG3 cold and dry climatic conditions had minor effects on the vegetational record of Tenaghi Phillippon (Fig. 12E) and on the hydrological and sedimentological processes of Lakes Prespa and Ohrid (Fig. 12C, D). More pronounced impacts during the LG3 glacial phase, are recorded on the vegetation distribution (reduction of *Pinus* and *Quercus* pollen, Fig. 12G, H) and on the sedimentation regime (Fig. 12 I, J decreasing fluvial inputs and coarsening trends of the sediments) of the north Aegean Sea borderlands. This zonal partitioning of glacial behavior during LG3, is also evident in marine and other terrestrial records with milder conditions to the Ionian and Adriatic Seas (the main source of moisture for Mount Tymphi) and colder and dryer conditions in the Aegean and Marmara Seas (Kothoff et al., 2011 and references therein).

The environmental conditions following LG3 during the Pleistocene–Holocene boundary recovered gradually towards the establishment of warm and wet climate. This change is reflected in a number of lacustrine and marine proxies among the few that are considered here (Fig. 12). These proxies include the gradual reduction of steppic taxa from 11.5 ka, and increasing productivity in Lakes Prespa, Ohrid, Dorjan (Aufgebauer et al., 2012, Vogel et al., 2010, Zhang et al., 2014) and in the Aegean Sea (Kothoff et al., 2008, 2011). A suite of marine proxies suggest lagged and stepwise increases in SST (Fig. 12F), precipitation, and river runoff (Fig. 12I) with peak values at 9.6 ka (Fig. 12I), contemporary with the glacier standstill phase HOL1 at 9.6 ± 1.2 ka (Fig. 10F, 11). The climatic thresholds responsible for HOL1 phase, are also responsible for the slow recovery of *Quercus* forests (Fig. 12H), for increasing fluvial inputs (Fig. 12I) and for a meltwater pulse in the north Aegean Sea (Fig. 12B) that reduced the surface salinities (Kothoff et al., 2008). In addition to the increasing fluvial runoff, this meltwater pulse was likely fostered through the preservance of the glacial ice and extensive permanent snowfields in the northeast Mediterranean mountains that resulted to subsequent discharge of both surface and karstic runoff during the melt out season, in agreement with Ehrmann et al. (2007). Once these climatic thresholds were surpassed at ~9.6 ka, complete deglaciation of the MK cirque occurred during the onset of Sapropel 1 formation (Kothoff et al., 2008).

Despite the fact that the mid-Holocene (9.5 – 3.0 ka) period has been characterized by considerable millennial and centennial-scale variability in terrestrial and marine systems of northeast Mediterranean (e.g. Rohling et al., 2002, Ehrmann et al., 2007, Kothoff et al., 2008, Tryantaphyllou et al., 2009, Schmiedl et al., 2010, Styllas and Ghilardi, 2017), no evidence of glacier fluctuations are represented in the ^{36}Cl chronology of MK cirque. These findings does thus not confirm the hypothesis postulated in our preceding work that the MK glaciers advanced during the mid-Holocene (Styllas et al., 2016). It is likely that the position of sea-level nearly at its present location (18km from the TZ and MK cirques) together with peak solar insolation, and high SST's and summer (mean July) air temperatures, are among the key factors that prohibited the return to glacier friendly conditions of sufficient duration to create glacial landforms in MK cirque. It has to be acknowledged that higher mean July air temperatures by 1-2^{o}C (Samartin et al., 2017), compared to our previously considered pollen-derived summer temperatures (gridded data by Mauri et al., 2015), may have also contributed to a "glacier free" mid Holocene on Mount Olympus. But, in the case that there had been glacier advance(s) during the mid-Holocene, they may be overridden by the subsequent late Holocene glacier expansions. The reduction of solar insolation during the Late Holocene (Fig. 12A), along with wet conditions between 3.3 and 2.6 ka recorded in the speleothem record of Skala Marion (Fig. 1), as well as in other eastern Mediterranean speleothem records (Psomiadis et al., 2018), are likely the main driving mechanisms of glacier expansion and stabilization of moraine MK-C3 at 2.5 ± 0.3 ka (Fig. 7) during HOL2 glacial phase (Figs 11 and 12). HOL2 is concomitant with a major soil erosion period recorded in the

geochemical and isotopic record of Lake Dorjan (Fig. 1), (Rothacker et al., 2018); the authors ascribe this event to human activity, but given the wet and cold conditions that resulted to a glaciation phase, a combination of climatic and anthropogenic factors cannot be ruled out. HOL2 likely initiated around 2.8 ka during a major solar insolation low, the Homeric Minimum (Wirth and Sessions, 2016) and its duration matches the Bond 2 event (Bond et al., 2001), which like other Bond events during the Holocene, has been found to correspond to periods of high hydrologic activity of the Aliakmon River (Fig. 1) (Styllas and Ghilardi, 2017). Therefore, it is plausible that the climatic and environmental conditions during HOL2, with a glacier expanse in Megala Kazania cirque and a local ELA of 2250m, were associated with the existence of permanent snowfields in the Throne of Zeus cirque and other locations above the local ELA. This might have fed the imaginations of the Ancient Greeks and may have given Mount Olympus its name ("*Ολό-λαμπος*"), which means the "ever shining mountain" (Curtius, 1879). Homer himself refers to Mount Olympus permanent snows in many occasions in both ancient Greek poems of Iliad and Odyssey (Nezis, 2000). From a paleoclimatic standpoint, glacial phase HOL2 exhibits special interest, as it can provide quantitive estimates on annual precipitation and temperature during a period when human activities were intense enough to alter the pollen composition of lacustrine and marine records, obscuring the paleoclimatic information (e.g. Kothoff et al., 2008, Vogel et al., 2010, Kothoff et al., 2011, Aufgebauer et al., 2012, Francke et al., 2013, Zhang et al., 2014, Pross et al., 2015, Rothacker et al., 2018, Wulf et al., 2018).
The last phase of glacial activity depicted from our SED chronology (HOL3) is derived from blocky moraine MK-C4, which is located 100m below the present-day terminus of Mount Olympus extant snowfields (Fig. 5). HOL3 occurred at 0.64 ± 0.08 ka (AD 1320 – 1480) during the latter part of the Medieval Climate Anomaly (MCA) and the early part of the Little Ice Age (LIA), a transition that in Eastern Mediterranean was characterized by a shift from wet to dry conditions (Roberts et al., 2012). Even though HOL-3 is constrained by only one SED, tree-ring proxy data from Mount Olympus, point to warmer than present summer (June – September) temperatures between AD 1500 – 1700 (Klesse et al., 2014) and this trend is also reflected in the north Aegean Sea SST record (Gogou et al., 2016). Higher than present summer temperatures and increased SST's, on Mount Olympus and the north Aegean Sea, were coupled by regional aridity as manifested by the decrease of allochthonous sediments in Lake Dorjan (Francke et al., 2013) around AD 1550 and the combination of these conditions most likely triggered the early LIA glacier retreat of Megala Kazania paleoglacier. A reverse signal is observed in the western Balkans, as the interval between AD 1500 – 1800, is characterized by wet climatic conditions (Morellón et al., 2016, Koutsodendris et al., 2017). HOL3 and LG3 glacial phases, emphasize the existence of an E-W climatic partitioning along the southern Balkan Peninsular, evident in the Mediterranean basin during the last millennium (Roberts et al., 2012), but the boundary of this see-saw climatic pattern needs to be better defined by additional proxy-based studies (Koutsodendris et al., 2017), including the glacial record.

6. Conclusions

In this study, we propose a new Late-glacial and Holocene chronology of glacial phases of Mount Olympus and compare it with existing SED based glacier chronologies from the northeast Mediterranean mountains. Our glacial chronology is based on *in situ*-produced ^{36}Cl-based cosmic ray exposure dating of 20 glacially transported boulder and bedrock samples from the east facing Throne of Zeus (TZ) and northwest oriented Megala Kazania (MK) cirques, which are consistent with the stratigraphic positions of the geomorphologically distinct frontal, push, hummocky and blocky moraines. The new glacial chronology from Mount Olympus is complementary, but greatly refines the existing SED-based glacier chronologies from Mount Pelister, Galicica Mountains, Šara Range, Rila Mountains and Mount Uludağ.
The first Late-glacial phase of glacial variability (LG1) is characterized by moraine stabilization at ~15.5 ka under overall dry and cold conditions, followed by deglaciation due to increasing temperatures and precipitation during its later stage at ~14.0 ka. Solar insolation maxima and low precipitation during LG1, likely restricted the glacier expansions within the higher cirques and at elevations between 2000 and 2200m. The climatic conditions that followed LG1, are characterized by considerable increases in precipitation and temperature, but in the highest cirques of Mount Olympus such increases were less pronounced and forced a shift to marginally glacial conditions with intense aeolian activity from western directions and solar insolation minima at ~13.5 ka during LG2. A sharp drop in precipitation, air temperatures and north Aegean SST's marked the beginning of phase LG3 with immediate impacts on the high cirques of the northeast Mediterranean mountains, which experienced a return to glacial conditions at ~12.5 ka. On Mount Olympus,

LG3 was expressed by a significant drop in air temperatures and overall glacier shrinking, whereas milder and/or drier conditions occurred to the west of the Pindos Mountains (southwestern Balkans). Within error uncertainties of our new SED and mean landform ages, glacial phases LG1-3 can be tentatively correlated to the Older Dryas, Bölling/Alleröd and Younger Dryas periods of the Greenland isotope record.

The Pleistocene / Holocene transition saw a gradual and stepwise return to milder conditions that are recorded in a large array of lacustrine and marine proxies. Above 2000m, the deglaciation followed the reorganization of the atmosphere, as high precipitation amounts and cooler summer temperatures likely forced a glacier standstill or re-advance phase (HOL1) at ~9.6 ka, followed by the onset of very humid and warm conditions in the north Aegean Sea. The mid-Holocene glacial evolution was likely characterized by complete deglaciation, in phase with high summer temperatures and solar insolation. A decline in solar insolation combined with climate deteriorations associated with North Atlantic's Bond Events, resulted in a glacier expansion in Megala Kazania cirque during the late Holocene (HOL2). The initiation of phase HOL2 might have started around 2.8 ka during the Homeric solar low, combined with wet conditions and subsequent moraine stabilization occurred at ~2.5 ka. The last phase of glacial activity on Mount Olympus as well as on other northeast Mediterranean mountains (HOL3) was less extensive than HOL2 and was restricted close to the cirque headwalls. Phase HOL3 corresponds to the end of the Medieval Climate Anomaly and the beginning Little Ice Age, as evidenced from one boulder dated to ~0.6 ka.

In summary, we present here for the first time a glacial chronology of the northeast Mediterranean mountains that spans the Late Glacial and the Holocene and is consistent with a number of terrestrial and marine proxies. An *out-of-phase* behaviour between the a solar insolation peak and glacial phases is observed during the Late-glacial, but this pattern gets back into phase during the Holocene, as glacial phases occur during solar insolation lows. We show that in addition to the early Little Ice Age glacier advance, two Holocene glacial phases are recorded in the glacial geomorphology on Mount Olympus, during the early and late Holocene. In comparison with the other cirques under consideration, these Holocene glacial phases were more pronounced in Megala Kazania cirque due to its topographic characteristics and proximity to the north Aegean Sea.

Acknowledgements

This work was financed by the Scientific Studies Program of John S. Latsis Foundation, Athens, Greece. The French AMS national facility ASTER (CEREGE, Aix en Provence) is supported by the INSU/CNRS, the ANR through the "Projets thématiques d'excellence" program for the "Equipements d'excellence" ASTER-CEREGE action and IRD. Michael Styllas is particularly thankful to Basil Davis (Université de Lausanne) and to Stefan Klesse (University of Arizona) for their fruitful discussions, commends and data sharing during the course of the project "Did the Ancient Greek Gods Ever Got Cold? Examining the Holocene Glacial History of Mount Olympus, Greece". We are thankful to two anonymous reviewers for their constructive comments that further improved the manuscript.

References

Akçar, N., Yavuz, V., Ivy-Ochs, S., Reber, R., Kubik, P.W., Zahno, C. & Schlüchter, C., 2014. Glacier response to changes in atmospheric circulation in the eastern Mediterranean during the Last Glacial Maximum. Quat. Geochronol. 19, 27–41.

Akçar, N., Ivy-Ochs, S., Kubik, P.W., Schlüchter, C., 2011. Post-depositional impacts on 'Findlinge' (erratic boulders) and their implications for surface-exposure dating. Swiss Journal of Geosciences 104, 445-453.

Alley, R.B., 2000. The Younger Dryas cold interval as viewed from central Greenland. Quat. Sci. Rev. 19, 213–226.

Arnold, M., Aumaître, G., Bourlès, D.L., Keddadouche, K., Braucher, R., Finkel, R.C., Nottoli, E., Benedetti, L., Merchel, S., 2013. The French accelerator mass spectrometry facility ASTER after 4 years: Status and recent developments on ^{36}Cl and ^{129}I. Nuclear Instruments and Methods in Physics Research (B) 294, 24–28.

Aufgebauer, A., Panagiotopoulos, K., Wagner, B., Schaebitz, F., Viehberg, F.A., Vogel, H., Zanchetta, G., Sulpizio, R., Leng, M.J., Damaschke, M., 2012. Climate and environmental change in the Balkans over the last 17 ka recorded in sediments from Lake Prespa (Albania/F.Y.R. of Macedonia/Greece). Quat. Int. 274, 122-135.

Balco, G., Stone, J., Lifton, N., Dunai, T., 2008. A complete and easily accessible means of calculating surface exposure ages or erosion rates from 10Be and 26Al measurements. Quat. Geochronol. 3, 174-195.

Balco, G., Briner, J., Finkel, R.C., Rayburn, J.A., Ridge, J.C., Schaefer, J.M., 2009. Regional beryllium-10 production rate calibration for late-glacial northeast- ern North America. Quat. Geochronol. 4, 93–107. http://dx.doi.org/10.1016/ j.quageo.2008.09.001.

Balco, G., 2011. Contributions and unrealized potential contributions of cosmogenic-nuclide exposure dating to glacier chronology. 1990-2010. Quat. Sci. Rev. 30, 3–27.

Bartzokas, A., Lolis, C.J., Metaxas, C.A., 2003. The 850mb relative vorticity centres of action for winter precipitation in the Greek area. Int. J. Climatol. 23, 813 – 828.

Berger, A., Loutre, M.F., 1991. Insolation values for the climate of the last 10 million years. Quat. Sci. Rev. 10, 297-317.

Bond, G., Kromer, B., Beer, J., Muscheler, R., Evans, M.N., Showers, W., Hoffmann, S., Lotti-Bond, R., Hajdas, I., Bonani, G., 2001. Persistent solar influence on North Atlantic climate during the Holocene. Science 294, 2130–2136.

Bordon, A., Peyron, O., Lézine, A.-M., Brewer, S., Fouache, E. 2009. Pollen-inferred Late-Glacial and Holocene climate in southern Balkans (Lake Maliq). Quat. Int. 200, 19-30.

Bouchez C., Pupier J., Benedetti L., Deschamps P., Guillou V., Keddadouche K., Aumaître G., Arnold M., Bourlès D. (2015) Isotope Dilution-AMS technique for ^{36}Cl and Cl determination in low chlorine content waters, Chem. Geol. 404, 62-70.

Braucher, R., Merchel, S., Borgomano, J., Bourlès, D.L., 2011. Production of cosmogenic radionuclides at great depth: A multi element approach. Ear. Plan. Sci. Let. 309, 1-9.

Curtius, G., 1879. Grundzüge der griechischen Etymologie. 5th Edition, Leipzig, p. 265.

Delunel, R. Bourlès, D.L., van der Beek, P.A., Schlunegger, F., Leya, I., Masarik, J., Paquet, E., 2014. Snow shielding factors for cosmogenic nuclide dating inferred from long-term neutron detector monitoring. Quat. Geochronol. 24, 16–26.

Digerfeldt, G., Sandgren, P. & Olsson, S., 2007. Reconstruction of Holocene lake-level changes in Lake Xinias, central Greece. Holocene 17(3), 361–367.

Domíniguez-Villar, D., Carracasco, R.M., Pedrazza, J., Cheng, H., Edwards, R.L., Willenbring, J.K., 2013. Early maximum extend of paleoglaciers from Mediterranean mountains during the last glaciation. Sci. Rep. 3, 2034.

Dunai, T. J., Binnie, S. A., Hein, A, S., Paling, S. M. 2014. The effects of a hydrogen-rich ground cover on cosmogenic thermal neutrons: Implications for exposure dating. Quat. Geochronol. 22, 183-191.

Ehrmann, W., Schmiedl, G., Hamann, Y., Kuhnt, T., Hemleben, C., Siebel, W., 2007. Clay minerals in Lateglacial and Holocene sediments of the northern and southern Aegean Sea. Palaeog. Palaeoclim. Palaeoec. 249, 36–57.

Flockas, H.A., Karakostas, T.S., 1996. Cyclogenesis over the Aegean Sea: Identification and synoptic categories. Meteorol. Appl. 3, 53 – 61.

Francke, A., Wagner, B., M. Leng, M.J., and Rethemeyer, J., 2013. A Late-Glacial to Holocene record of environmental change from Lake Dorjan (Macedonia, Greece). Clim. Past 9, 481–498.

Gogou, A., Bouloubassi, I., Lykousis, V., Arnaboldi, M., Gaitani, P., Meyers, P.A., 2007. Organic geochemical evidence of abrupt late glacial-Holocene climate changes in the North Aegean Sea. Palaeog. Palaeoclim. Palaeoec. 256, 1–20.

Gogou, A., Triantaphyllou, M., Xoplaki, E., Izdebski, A., Parinos, C., Dimiza, M., Bouloubassi, I., Luterbacher, J., Kouli, K., Martrat, B., Toreti, A., Fleitmann, D., Rousakis, G., Kaberi, H., Athanasiou, M., Lykousis, V., 2016. Climate variability and socio-environmental changes in the northern Aegean (NE Mediterranean) during the last 1500 years. Quat. Sci. Rev. 209–228.

González-Trueba, J.J., Martín-Moreno, R., Martínezde-Pisón, E., Serrano, E., 2008. Little Ice Age glaciation and current glaciers in the Iberian Peninsula. Holocene 18, 551–568. doi:10.1177/0959683608089209.

Gromig, R., Mechenrich, S., Ribolini, A., Wagner, B., Zanchetta, G., Isola, I., Bini, M., Dunai, T.J., 2017. Evidence for a Younger Dryas deglaciation in the Galicica Mountains (FYROM) from cosmogenic ^{36}Cl. Quat. Int., http://dx.doi.org/10.1016/j.quaint.2017.07.013.

Hamann, Y., Ehrmann, W., Schmiedl, G., Krüger, S., Stuut, J.B., Kuhnt, T., 2008. Sedimentation processes in the eastern Mediterranean Sea during the Late Glacial and Holocene revealed by end-member modelling. Mar. Geol. 248, 97–114.

Hughes, P.D., Gibbard, P.L. and Woodward, J.C., 2003. Relict rock glaciers as indicators of Mediterranean palaeoclimate during the Last Glacial Maximum (Late Würmian) of northwest Greece. J. Quat. Sci. 18, 431-440.

Hughes, P.D., Woodward, J.C., Gibbard, P.L., 2006a. Late Pleistocene glaciers and climate in the Mediterranean region. Glob. Plan. Change 46, 83–98.

Hughes, P.D., Woodward, J.C., Gibbard, P.L. 2006b. The last glaciers of Greece. Z. Geom. 50, 37–61.

Hughes, P.D., 2009. Twenty-first century glaciers and climate in the Prokletije Mountains, Albania. Arct. Antarct. Alp. Res. 41, 455–459. Doi: 10.1657/1938- 4246-41.4.455.

Hughes, P.D., Gibbard, P.L., 2015. A stratigraphical basis for the Last Glacial Maximum (LGM). Quat. Int. 383, 174–185.

Hughes, P.D., Woodward, J.C., 2017. Quaternary glaciation in the Mediterranean: a new synthesis. In: Hughes, P.D. & Woodward, J.C. (Eds) Quaternary Glaciation in the Mediterranean Mountains. Geological Society, London, Special Publications, 433, 1–23, https://doi.org/10.1144/SP433.14

Hambrey, M., Huddart, D., Bennet, M.R., Glasser N.F., 1997. Genesis of 'hummocky moraines' by thrusting in glacier ice: evidence from Svalbard and Britain. J. Geol. Soc. Lon. 154, 623–632.

Huss, M., Fischer M., 2016. Sensitivity of very small glaciers in the Swiss Alps to climate change. Frontiers in Earth Science. doi: 10.3389/feart.2016.00034.

Imbrie, J., Berger, A., Boyle, E.A., Clemens, S.C., Duffy, A., Howard, W.R., Kukla, G., Kutzbach, J., Martinson, D.G., McIntyre, A., Mix, A.C., Molfino, B., Morley, J.J., Peterson, L.C., Pisias, N.G., Prell, W.L., Raymo, M.E., Shackleton, N.J., Toggweiler, J.R., 1993. On the structure and origin of major glaciation cycles. 2. The 100,000-year cycle. Paleoceanography, 8(6), 699–735.

Ivy-Ochs, S., Synal, H.A., Roth, C., Schaller, M., 2004. Initial results from isotope dilution for Cl and Cl-36 measurements at the PSI/ETH Zurich AMS facility. Nucl. Instrum. Methods Phys. Res. Sect. B Beam Interact. Mater. Atoms 223–224, 623–627.

Karkanas, P., 2001. Site Formation Processes in Theopetra Cave: A Record of Climatic Change during the Late Pleistocene and Early Holocene in Thessaly, Greece. Geoarchaeol. 16, 4, 373 – 399.

Klesse, S., Ziehmer, M., Rousakis, G., Trouet, V., Frank, D., 2015. Synoptic drivers of 400 years of summer temperature and precipitation variability on Mt. Olympus, Greece. Clim. Dyn. 45, 807–824.

Kotthoff, U., Pross, J., Muller, U.C., Peyron, O., Schmiedl, G., Schlutz, H., Bordon, A., 2008. Climate dynamics in the borderlands of the Aegean Sea during deposition of Sapropel S1 deduced from a marine pollen record. Quat. Sci. Rev., 27, 832–845.

Kotthoff, U., Koutsodendris, A., Pross, J., Schmiedl, G., Bornemann, A., Kaul, C., Marino, G., Peyron, O., Schiebel, R., 2011. Impact of Lateglacial cold events on the northern Aegean region reconstructed from marine and terrestrial proxy data. J. Quat. Sci. 26, 86-96.

Kubik, P. W., Christl, M., 2010. 10Be and 26Al measurements at the Zurich 6 MV tandem AMS facility. Nuclear Instruments and Methods in Physics Research B, 268, 880–883.

Kuhlemann, J., Rohling, E.J., Krumrei, I., Kubik, P., Ivy-Ochs, S. & Kucera, M., 2008. Regional synthesis of Mediterranean atmospheric circulation during the last glacial maximum. Science, 321, 1338–1340.

Kuhlemann, J., Milivojević, M., Krumrei, I. & Kubik, P.W., 2009. Last glaciation of the Sara range (Balkan Peninsula): Increasing dryness from the LGM to the Holocene. Austrian Journal of Earth Science, 102, 146–158.

Kuhlemann, J., Gachev, E., Gikov, A., Nedkov, S., Krumrei, I. & Kubik, P., 2013. Glaciation in the Rila Mountains (Bulgaria) during the Last Glacial Maximum. Quat. Int., 293, 51–62.

Koutsodendris, A., Brauer, A., Reed, J.M., Plessen, B., Friedrich, O., Hennrich, B., Zacharias, I., Pross, J., 2017. Climate variability in SE Europe since 1450 AD based on a varved sediment record from Etoliko Lagoon (Western Greece). Quat. Sci. Rev. 159, 63–76.

Lambeck, K., 1996. Sea-level change and shore-line evolution in Aegean Greece since Upper Palaeolithic time. Antiquity, 70.

Lambeck, K., Rouby, H., Purcell, A., Sun, Y., Sambridge, M., 2014. Sea level and global ice volumes from the Last Glacial Maximum to the Holocene. PNAS, 111(43), 15296–15303. doi:10.1073/pnas.1411762111/-/DCSupplemental.

Lawson, I., Frogley, M., Bryant, C., Preece, R., Tzedakis, P.C., 2004. The Lateglacial and Holocene vegetation history of the Ioannina basin, north-west Greece. Quat. Sci. Rev., 23, 1599-1625.

Lawson, I.T., Al-Omari, S., Tzedakis, P.C., Bryant, C.L., Christianis, K., 2005. Lateglacial and Holocene vegetation history at Nisi Fen and the Boras mountains, northern Greece. Holocene 15, 873–337.

Manz, L.A., 1998. Cosmogenic ^{36}Cl chronology for deposits of presumed Pleistocene age on the Eastern Piedmont of Mount Olympus, Pieria, Greece. Unpublished MSc thesis, Ohio University.

Marino, G., Rohling, E.J., Sangiorgi, F., Hayes, A., Casford, J. L., Lotter, A. F., Kucera, M., Brinkhuis, H., 2009. Early and middle Holocene in the Aegean Sea: interplay between high and low latitude climate variability. Quat. Sci. Rev. 28, 3246–3262.

Masarik, J., Kim, K. J., Reedy, R. C. 2007. Numerical simulations of in situ production of terrestrial cosmogenic nuclides. Nuclear Instruments and Methods in Physics Research, section B: Beam Interactions with Materials and Atoms 259, 642-645.

Mauri, A., Davies, B.A.S., Collins, P.M., Kaplan, J.O. 2015. The climate of Europe during the Holocene: a gridded pollen-based reconstruction and its multi-proxy evaluation. Quat. Sci. Rev. 112, 109–127.

Marrero, S. M., Phillips, F. M., Caffee, M. W., Gosse, J. C. 2016. CRONUS-Earth cosmogenic ^{36}Cl calibration. Quat. Geochronol. 31, 199-219.

Merchel, S., Bremser, W., Alfimov, V., Arnold, M., Aumaître, G., Benedetti, L., Bourles, D.L., Caffee, M., Fifield, L.K., Finkel, R.C., Freeman, S.P.H.T., Martschini, M., Matsushi, Y., Rood, D.H., Sasa, K., Steier, P., Takahashi, T., Tamari, M., Tims, S.G., Tosaki, Y., Wilcken, K.M., Xu, S., 2011. Ultra-trace analysis of 36Cl by accelerator mass spectrometry: an interlaboratory study. Anal. Bio- anal. Chem., 400(9), 3125–3132 https://doi.org/10.1007/s00216-011-4979-2.

Morellón, M., Anselmetti, F.S., Ariztegui, D., Brushulli, B., Sinopoli, G., Wagner, B., Sadori, L., Gilli, A., Pambuku, A., 2016. Human-climate interactions in the central Mediterranean region during the last millennia: the laminated record of Lake Butrint (Albania). Quat. Sci. Rev. 136, 134–152.

Nezis, N., 2000. Olympos (*in Greek*). Eds. Anavasi, ISBN 13, 9789608195578.

Oerlemans, J., 2005. Extracting a climate signal from 169 glacier records. Science 308, 675–677.

Perissoratis, C. and Conispoliatis, N., 2003. The impacts of sea level changes during the latest Pleistocene and Holocene times on the morphology of Ionian and Aegean seas (SE Alpine Europe). Mar. Geol. 196, 145–156.

Peyron, O., Guiot, J., Cheddadi, R., Tarasov, P., Reille, M., de Beaulieu, J-L., Bottema, S. and Andrieu, V., 1998. Climatic reconstruction in Europe for 18,000 YR B.P. from Pollen Data. Quat. Res. 49, 183-196.

Phillips, F.M., Stone, W.D., Fabryka-Martin, J.T., 2001. An improved approach to calculating low-energy cosmic-ray neutron fluxes near the land/atmosphere interface. Chem. Geol. 175, 689-701.

Pope, R.J., Hughes, P.D., Skourtsos, E., 2015. Glacial history of Mt Chelmos, Peloponnesus, Greece. In: Hughes, P.D. & Woodward, J.C. (eds) Quaternary Glaciation in the Mediterranean Mountains. Geological Society, London, Special Publications, 433, 211–236, https://doi.org/10.1144/SP433.11.

Porter, S.C., 2001. Snowline Depression in the Tropics during the Last Glaciation. Quat. Sci. Rev. 20, 1067-1091.

Pross, J., Kotthoff, U., Müller, U.C., Peyron, O., Dormoy, I., Schmiedl, G., Kalaitzidis, S., and Smith, A., 2009. Massive perturbation in terrestrial ecosystems of the Eastern Mediterranean region associated with the 8.2 kyr climatic event. Geology, 37, 887–890.

Pross, J., Koutsodendris, A., Christanis, K., Fischer, T., Fletcher, W.J., Hardiman, M., Kalaitzidis, S., Knipping, M., Kotthoff, U., Milner, A.M., Müller, U.C., Schmiedl, G., Siavalas, G., Tzedakis, P.C., Wulf, S., 2015. The 1.35-Ma-long terrestrial climate archive of Tenaghi Philippon, northeastern Greece: Evolution, exploration, and perspectives for future research. Newsletters on Stratigraphy 48, 253-276.

Psomiadis, D., Dotsika, E., Albanakis, K., Ghaleb, B., Hillaire – Marcel, C., 2018. Speleothem record of climatic changes in the northern Aegean region (Greece) from the Bronze Age to the collapse of the Roman Empire. Palaeog. Palaeoc. Palaeoec. Doi:10.1016/j.palaeo.2017.10.021.

Putkonen, J., Swanson, T., 2003. Accuracy of cosmogenic ages for moraines. Quat. Res., 59, 255-261.

Rohling, E.J., Mayewski, P.A., Abu-Zied, R.H., Casford, J.S.L., Hayes, A., 2002a. Holocene atmosphere-ocean interactions: records from Greenland and the Aegean. Clim. Dyn. 18, 587–593.

Rasmussen, S. O., Andersen, K. K., Svensson, A. M., Steffensen, J. P., Vinther, B. M., Clausen, H. B., Siggaard-Andersen, M.-L., Johnsen, S. J., Larsen, L. B., Dahl-Jensen, D., Bigler, M., Röthlisberger, R., Fischer, H., Goto-Azuma, K., Hansson, M. E., Ruth, U., 2006. A new Greenland ice core chronology for the last glacial termination. J. Geophys. Res. 111, D06102, doi: 10.1029/2005JD006079.

Roberts, N., Moreno, A., Valero-Garcés, B.L., Corella, J.P., Jones, M., Allcock, S., Woodbridge, J., Morellón, M., Luterbacher, J., Xoplaki, E., Türkes, M., 2012. Palaeolimnological evidence for an east-west climate see-saw in the Mediterranean since AD 900. Glob. Planet. Change 84–85, 23–34.

Rothacker, L., Dosseto, A., Francke, A., Chivas, A., Vigier, N., Kotarba-Morley, A.M., Menozzi, D., 2018. Impact of climate change and human activity on soil landscapes over the past 12,300 years. Scientific Reports, 8, 247 (DOI:10.1038/s41598-017-18603-4).

Ribolini, A., Bini, M., Isola, I., Spagnolo, M., Zanchetta, G., Pellitero, R., Mechernich, S., Gromig, R., Dunai, T.J., Wagner, B., Milevski, I., 2017. An Oldest Dryas glacier expansion on Mount Pelister (Former Yugoslavian Republic of Macedonia) according to ^{10}Be cosmogenic dating. J. Geol. Soc. Lond. http://dx.doi.org/10.1144/jgs2017-038.

Ryan, W.B.F., Carbotte, S.M., Coplan, J.O., O'Hara, S., Melkonian, A., Arko, R., Weissel, R.A., Ferrini, V., Goodwillie, A., Nitsche, F., Bonczkowski, J., Zemsky, R., 2009. Global Multi-Resolution Topography synthesis, Geochem. Geophys. Geosyst. 10, Q03014, doi: 10.1029/2008GC002332.

Samartin, S., Heiri, O., Joos, F., Renssen, H., Franke, J., Brönnimann, S., Tinner, W., 2017. Warm Mediterranean mid-Holocene summers inferred from fossil midge assemblages. Nature Geoscience, 10, 207–212, DOI: 10.1038/NGEO2891.
Scapozza, C., 015. Investigation of protalus ramparts in the Swiss Alps. Geogr. Helv., 70, 135–139.

Schlagenhauf, A., Gaudemer, Y., Benedetti, L., Manighetti, I., Palumbo, L., Schimmelpfennig, I., Finkel, R., Pou, K., 2010. Using in situ Chlorine-36 cosmonuclide to recover past earthquake histories on limestone normal fault scarps: a reappraisal of methodology and interpretations. Geoph. J. Int. 182(1), 36–72.

Schimmelpfennig, I., Benedetti, L, Finkel, R., Pik, R., Biard, P.-H., Bourles, D., Burnard, P., Williams, A., 2009. Sources of in-situ 36Cl in basaltic rocks. Implic. Calibration Prod. Rates Quat. Geochronol. 6, 441-461.

Schimmelpfennig, I., Benedetti, L, Garreta, V., Pik, R., Blard, P.-H., Burnard, P., Bourles, D., Finkel, R., Ammon, K., Dunai, T., 2011. Calibration of cosmogenic 36CI production rates from Ca and K spallation in lava flows from Mt. Etna (38^{o} N, Italy) and Payun Matru (36^{o} S, Argentina). Geochim. Cosmochim. Acta 75, 2611-2632.

Schmiedl, G., Kuhnt, T., Ehrmann, W., Emeis, K-C., Hamann, Y., Kothoff, U., Dulski, P., Pross, J., 2010. Climatic forcing of eastern Mediterranean deep-water formation and benthic ecosystems during the past 22 000 years. Quat. Sci. Rev. 29, 3006–3020.

Shakesby, R.A., Dawson, A.G. & Matthews. J.A., 1987. Rock glaciers, protalus ramparts and related phenomena, Rondane, Norway: a continuum of large-scale talus-derived landforms. Boreas 16, 305-317.

Smith, G.W., Nance, R.D., Genes, A.N., 1997. Quaternary glacial history of Mount Olympus. Geol. Soc. Am. Bull. 109, 809– 824.

Smith, G.W., Nance, R.D. & Genes, A.N., 2006. Pleistocene glacial history of Mount Olympus, Greece: Neotectonic uplift, equilibrium line elevations, and implications for climatic change. Geological Society of America Special Papers 409, 157 - 174.

Stone, J.O., Allan, G.L., Fifield, L.K., Cresswell, R.G., 1996. Cosmogenic chlorine-36 from calcium spallation. Geochim. Cosmochim. Acta, 60 (4), 679 – 692.

Stone, J.0., 2000. Air pressure and cosmogenic isotope production. J. Geophys. Res. 105, 23753-23759.

Stoykova, D.A., Shopov, Y.Y., Garbeva, D., Tsankov, L.T., Yonge, C.J. 2008. Origin of the climatic cycles from orbital to sub-annual scales. J. Atm. Sol. Ter. Phy. 70, 293–302.

Styllas, M., Schimmelpfennig, I, Benedetti, L., Ghilardi, M., 2016. Geomorphologic and paleoclimatic evidence of Holocene glaciation on Mount Olympus, Greece. Holocene 26(5), 709–721.

Styllas, M. and Ghilardi, M. 2017. Early to mid-Holocene paleohydrology in northeast Mediterranean: The detrital record of Aliakmon River in Lake Loudias, Greece. Holocene 27(10), 1487–1498.

Triantaphyllou, M.V., Ziveri, P., Gogou, A., Marino, G., Lykousis, V., Bouloubassi, I., Emeis, K.C., Kouli, K., Dimizia, M., Rosell-Mele, A., Papanikolaou, M., Katsouras, G., Nunez, N., 2009. Late GlacialeHolocene climate variability at the south-eastern margin of the Aegean Sea. Mar. Geol. 266, 182–197.

Tzedakis, P.C., Palike, H., Roucoux, K.H., de Abreu, L. 2009. Atmospheric methane, southern Europe vegetation and low mid-latitude links on orbital and millennial time scales. Ear. Plan. Sci. Let. 277(3–4), 307–371.

Vogel, H., Zanchetta, G., Sulpizio, R., Wagner, B., Nowaczyk, N., 2010b. A tephrostratigraphic record for the last glacial-interglacial cycle from Lake Ohrid, Albania and Macedonia. J. Quat. Sci. 25, 320–338.

Wagner, B., Aufgebauer, A., Vogel, H., Zanchetta, G., Sulpizio, R., Damasckhe, M., 2012. Late Pleistocene and Holocene contourite drift in Lake Prespa (Albania/F.Y.R. of Macedonia/Greece). Quat. Int. 274, 112-121.

Walker, M.J.C., Berkelhammer, L., Björck, S., Cwynar, L.C., Fisher, D.A., Long, A.J., Lowe, J.J., Newnham, R.M., Rasmussen, C.O., Weiss, H., 2012. Formal subdivision of the Holocene Series/Epoch: a Discussion Paper by a Working Group of INTIMATE (Integration of ice-core, marine and terrestrial records) and the Subcommission on Quaternary Stratigraphy (International Commission on Stratigraphy). J. Quat. Sci., 27(7), 649–659.

Ward, G.K., Wilson, S.R., 1978. Procedures for comparing and combining radiocarbon age-determinations – critique. Archaeometry 20, 19-31.

Wirth, S.B. and Sessions, A.L. 2016. Plant-wax D/H ratios in the southern European Alps record multiple aspects of climate variability. Quat. Sci. Rev. 148, 176–181.

Wulf, S., et al. 2018. The marine isotope stage 1 – 5 cryptotephra record of Tenaghi Philippon, Greece: Towards a detailed tephrostratigraphic framework for the Eastern Mediterranean region. Quat. Sci. Rev. 186, 236–262.

Zahno, C., Akçar, N., Yavuz, V., Kubik, P.W., Schlüchter, C., 2010. Chronology of Late Pleistocene glacier variations at the Uludağ Mountain, NW Turkey. Quat. Sci. Rev. 29, 1173–1187.

Zhang, X., Reed, J., Wagner, B., Francke, A., Levkov, Z., 2014. Lateglacial and Holocene climate and environmental change in northeastern Mediterranean region: diatom evidence from Lake Dorjan (Republic of Macedonia/Greece). Quat. Sci. Rev. 103, 51 – 66.

Zweck, C., Zreda, M., Desilets, D., 2013. Snow shielding factors for cosmogenic nuclide dating inferred from Monte Carlo neutron transport simulations. Earth Plan. Sci. Let. 379, 64–71.